Surface Circulation in Block Island Sound and Adjacent Coastal and Shelf Regions: a FVCOM-CODAR Comparison

Yunfang Sun[1, 5], Changsheng Chen[1, 6], Robert C. Beardsley[2], Dave Ullman[3], Bradford Butman[4], Huichan Lin[1]

[1]School for Marine Science and Technology
University of Massachusetts Dartmouth
706 South Rodney French Blvd, New Bedford, MA 02744
Phone: 508-910-6355; E-mail: yfsun@mit.edu; c1chen@umassd.edu; hlin@umassd.edu

[2]Department of Physical Oceanography
Woods Hole Oceanographic Institution
Woods Hole, MA 02543
Phone: 508-289-2536; E-mail: rbeardsley@whoi.edu

[3]The Graduate School of Oceanography
University of Rhode Island
215 South Ferry Road, Narragansett, RI 02882
E-mail: dullman@mail.uri.edu

[4]Woods Hole Coastal and Marine Science Center
U.S. Geological Survey
384 Woods Hole Road, Woods Hole, MA 02543
E-mail: bbutman@usgs.gov

[5]Department of Earth, Atmospheric & Planetary Sciences
Massachusetts Institute of Technology
77 Massachusetts Avenue, Building 54-1417
Cambridge, Massachusetts 02139

[6]International Center for Marine Studies
Shanghai Ocean University, Shanghai, 201306, P. R. China

Citation: Sun, Y., C. Chen, R. C. Beardsley, D. Ullman, B. Butman and H. Lin, 2016, Surface circulations in Block Island Sound and adjacent coastal and shelf regions: A FVCOM-CODAR comparison, 143, 26-45, *Progress in Oceanography*, doi:10.1016/j.pocean.2016.02.005.

Abstract

CODAR-derived surface currents in Block Island Sound over the period of June 2000 through September 2008 were compared to currents computed using the Northeast Coastal Ocean Forecast System (NECOFS). The measurement uncertainty of CODAR-derived currents, estimated using statistics of a screened nine-year time series of hourly-averaged flow field, ranged from 3-7 cm/s in speed and 4°-14° in direction. The CODAR-derived and model-computed kinetic energy spectrum densities were in good agreement at subtidal frequencies, but the NECOFS-derived currents were larger by about 28% at semi-diurnal and diurnal tidal frequencies. The short-term (hourly to daily) current variability was dominated by the semidiurnal tides (predominantly the M_2 tide), which on average accounted for ~87% of the total kinetic energy. The diurnal tidal and subtidal variability accounted for ~4% and ~9% of the total kinetic energy, respectively. The monthly-averaged difference between the CODAR-derived and model-computed velocities over the study area was 6 cm/s or less in speed and 28° or less in direction over the study period. An EOF analysis for the low-frequency vertically-averaged model current field showed that the water transport in the Block Island Sound region was dominated by modes 1 and 2, which accounted for 89% and 7% of the total variance, respectively. Mode 1 represented a relatively stationary spatial and temporal flow pattern with a magnitude that varied with season. Mode 2 was characterized mainly by a secondary cross-shelf flow and a relatively strong along-shelf flow. Process-oriented model experiments indicated that the relatively stationary flow pattern found in mode 1 was a result of tidal rectification and its magnitude changed with seasonal stratification. Correlation analysis between the flow and wind stress suggested that the cross-shelf water transport and its

temporal variability in mode 2 were highly correlated to the surface wind forcing. The mode 2 derived onshore and offshore water transport, and was consistent with wind-driven Ekman theory. The along-shelf water transport over the outer shelf, where a large portion of the water flowed from upstream Nantucket Shoals, was not highly correlated to the surface wind stress.

1. Introduction

Block Island Sound is bounded to the southwest by Long Island, NY, to the southeast by Block Island, RI, and to the north by the Rhode Island coast (Figure 1). The Sound is open to Rhode Island Sound to the east, to Long Island Sound through the Race to the west, and to the shelf to the south through an opening between Block Island and Long Island. It is about 16 km wide and covers an area of ~600 km^2, with water depth varying from ~3 m near the coast to ~60 m in the region between Block Island and Long Island. As part of the Front-Resolving Observational Network with Telemetry (FRONT) project [*O'Donnell et al.*, 2005], three high-frequency (HF) Coastal Ocean Dynamics Application Radars (CODARs) were installed at Montauk Point on the eastern end of Long Island, NY, Southeast Light on Block Island, and on the southern coast of Rhode Island at Misquamicut (Figure 1). These radars, operating at transmit frequencies of ~25 MHz, have been providing surface current measurements since June 2000. Radial velocity estimates from each site are produced at hourly intervals using measured antenna patterns roughly within the sectors shown in Figure 1. The radial velocities are combined using the least-squares methodology of *Lipa and Barrick* [1983] on a grid with 1.5 km spacing. Vector currents and their

uncertainties are estimated using all available radial velocity estimates within a 2-km radius of each grid point. In this paper, we utilize surface current vector data from June 2000 through September 2008.

HF radars have been widely used to establish coastal ocean surface current observation systems in recent years [*Kim et al.*, 2011; *Holman and Haller*, 2013; *Paduan et al.*, 2013]. *Barrick* [2008a; b] established a theoretical basis of the HF radio sea scatter, which promoted this instrument in monitoring the surface currents in the coastal ocean and Great Lakes. *Graber et al.* [1997] made a direct comparison of HF radar-derived surface currents with in-situ current measurement data and reported that the error of radar-derived individual "perfect" radial velocity was on the order of ~7-8 cm/s and 15°-25°. *Liu et al.* [2014] compared CODAR and ADCP observations on the western Florida shelf and found the speed difference was on the order of ~5-9 cm/s. Within this measurement uncertainty, CODAR could be a reliable system to monitor surface currents in coastal regions characterized by relatively strong surface currents, for example, driven by tides, coastal buoyancy forcing, or storms. With broad spatial coverage and resolution similar to numerical models, CODAR-derived surface current fields have been used to assess ocean models. Examples can be seen in *Chao et al.* [2009] and *Shulman et al.* [2002; 2007] in Monterey Bay; *Dong et al.* [2009] in Santa Barbara Channel in the Southern California Bight; and *Mau et al.* [2008] in the Block Island Sound region. These studies qualitatively compared patterns of daily currents [e.g. *Shulman et al.*, 2002; 2007] or seasonal current variability [e.g. *Dong et al*., 2009].

A University of Massachusetts Dartmouth (UMASSD) and Woods Hole Oceanographic

Institution (WHOI) research team has established the unstructured-grid, Finite-Volume Community Ocean Model (FVCOM)-based global, regional, coastal, and estuarine nested model system in the US northeast coastal ocean (http://www.fvcom.smast.umassd.edu). The regional component of this system is named the Northeast Coastal Ocean Forecast System (NECOFS) and has been in quasi-operational mode at UMASSD since 2007. Based on the NECOFS framework, the FVCOM development team has conducted a 36-year (1978-2013) hindcast of the three-dimensional (3-D) current, water temperature, and salinity in the U.S. northeast coastal ocean that includes Block Island Sound. The availability of the nine-year CODAR dataset in Block Island Sound provided a unique opportunity to 1) assess the accuracy of the NECOFS hindcast field of surface currents at short-term (tidal periods and daily averaged) and longer-term (monthly and seasonal) time scales, and 2) use NECOFS to understand the physical mechanism(s) driving the spatial and temporal variability of the circulation in Block Island Sound and the adjacent coastal and shelf region.

There have been many observational and modeling studies of tides, currents, and water properties in Long Island Sound and the adjacent shelf region [*Beardsley and Boicourt*, 1981; *Ianniello*, 1981; *Hopkins and Dieterle*, 1983; 1987; *Blumberg and Galperin*, 1990; *Scheffner et al.*, 1994; *Blumberg and Prichard*, 1997; *Edwards et al.*, 2004; *Ullman and Codiga*, 2004; *Mau et al.*, 2008; *Lentz*, 2008; *O'Donnell et al.*, 2014]. These studies were primarily focused on Long Island Sound or the entire Mid-Atlantic Bight but included results in Block Island Sound. *Ullman and Codiga* [2004] combined two years of CODAR and ADCP current observations to examine

the seasonal variability of a coastal thermal front and the associated current jet in the Long Island Sound outflow region. *Mau et al.* [2008] applied the Princeton Ocean Model (POM) to Block Island Sound and ran it for 2001 with assimilation of salinity and temperature data. They compared the model-computed and CODAR-derived annual mean flows and first and second Empirical Orthogonal Function (EOF) modes. The model showed reasonable agreement in the annual mean flow comparison. No model-CODAR comparisons have been made to examine interannual variability by using multiyear continuous CODAR measurements in the Block Island Sound region.

In this paper, we compare the NECOFS-hindcast flow field to the available CODAR data in Block Island Sound for the time period from June 2000 through September 2008. Several questions are addressed in this study. First, within a known measurement uncertainty, what time scale and spatial flow variability could NECOFS capture? Second, CODAR surface current estimates are based on Bragg backscatter from roughly 6-m long surface waves. The interaction of these surface waves with the surface currents could produce a radiation stress and modify the lower-frequency flow field. Could this wave-current interaction affect the model's surface circulation results, and if so, at what level? Third, how was the flow in the semi-enclosed Block Island Sound affected by Block Island and Long Island?

2. The Data and Model

2.1 CODAR Data

The surface current data used in this study were derived from three CODARs covering the Block Island Sound region (Figure 1). The effective depth of the surface current estimates from these systems is approximately the upper 0.5 m of the water column [*Stewart and Joy*, 1974]. The measurements covered an area of about 70 × 65 km including an along-shelf region extending from Long Island Sound to Block Island and a cross-shelf region from the coast to the 60-m isobath (Figure 1). The CODAR measurement system produced hourly averages of radial currents in spatial bins with range resolution of 1.5 km and azimuthal resolution of 5º. The CODAR software computed 10-minute averages and then "merged" them using the median value within each spatial bin over a one-hour time interval [*Ullman and Codiga*, 2004]. The hourly radial current measurements were combined to produce vector current estimates on a 46 × 43 grid (Figure 2).

A nine-year CODAR dataset collected from June 2000 through September 2008 was used in this study. Due to fluctuations in environmental conditions and operational issues, not all grid points had continuous and good quality time series. There were 1147 grid points, which contained some data (Figure 2). A CODAR 'system down' period was defined as a month when the percentage of available hourly data across all grid cells was less than 20%; otherwise the system was considered 'on'. Only measurements made during the 'system on' months were used in this

study. In order to select high-quality measurements within 'system on' periods, the data were screened using the following criteria: 1) the current speed magnitude uncertainty was no larger than 10.0 cm/s; 2) the current direction uncertainty was no larger than 30º; and 3) the number of radial velocities used in the CODAR data processing was no smaller than 5. This screening process identified 334 grid points where the average percentage of good-quality data during 'system on' periods was larger than 60% (Figure 2). The model and CODAR data comparisons reported in this study were based on the data at these 334 grid points.

The nine-year hourly-averaged measurement uncertainty of CODAR-derived currents after data screening ranged from 3-7 cm/s in speed and 4°-14° in direction, and the monthly standard errors range from 1.5-3.5 cm/s in speed and 5°-38° in direction (Figure 3). The standard errors of the mean velocity and the mean direction are as follows:

$$SE_V^2 = \frac{1}{(\langle u\rangle^2+\langle v\rangle^2)}\left[\langle u\rangle^2 SE_u^2 + \langle v\rangle^2 SE_v^2 + 2\langle u\rangle\langle v\rangle \frac{cov(u,v)}{N_{eff}}\right] \quad (1)$$

$$SE_\theta^2 = \frac{1}{(\langle v\rangle^2+\langle v\rangle^2)^2}\left[\langle v\rangle^2 SE_u^2 + \langle u\rangle^2 SE_v^2 - E\langle u\rangle\langle v\rangle \frac{cov(u,v)}{N_{eff}}\right] \quad (2)$$

where $\langle u\rangle$,$\langle v\rangle$ are the mean eastward and northward components of velocity; SE_u^2, SE_v^2 are the variances of these quantities; and N_{eff} is the effective degrees of freedom for the velocity magnitude (V) and direction (θ).

The uncertainty varied depending on location within the overlapping coverage areas of the three CODARs. The most accurate data were in the region covered by the effective ranges of all three CODARs. In regions covered by only two CODARs, the largest direction errors usually

occurred in the area around the line between the stations where only one component of current velocity could be resolved (for example between Montauk Point and Misquamicut).

2.2 NECOFS

The model-CODAR comparison was made using the NECOFS hourly hindcast field. NECOFS is a coupled atmospheric-ocean model system, with a mesoscale meteorological model (MM5 or WRF) [*Chen et al.*, 2005] for surface forcing, the Gulf of Maine FVCOM (GoM-FVCOM) [*Chen et al.*, 2011] for oceanic currents, temperature and salinity; and SWAVE [*Qi et al.*, 2009] for surface waves. MM5 is the fifth-generation NCAR/Penn State non-hydrostatic mesoscale model [*Dudhia et al.*, 2002] and WRF is the Weather Research and Forecast model [*Skamarock et al.*, 2008]. The surface forcing was created with a horizontal resolution of 9 km using MM5 for 1978-2006 and then using WRF with the same spatial resolution for 2007-2013.

FVCOM is the unstructured-grid Finite-Volume Community Ocean Model, which was originally developed by *Chen et al.* [2003] and improved by the joint UMASSD and WHOI FVCOM development team [*Chen et al.*, 2006; *Chen et al.*, 2013a]. The governing equations are discretized in an integral form over control volumes in which the advection terms are solved by a second-order accuracy upwind finite-volume flux scheme [*Kobayashi et al.*, 1999; *Hubbard*, 1999] with a time integration of either a mode-split solver or a semi-implicit solver. Mixing in FVCOM is parameterized using the General Turbulence Model (GOTM) [*Burchard*, 2002] in the vertical and the Smagorinsky turbulent parameterization [*Smagorinsky*, 1963] in the horizontal.

SWAVE is an unstructured grid version of SWAN that was implemented into FVCOM [*Qi et al.*, 2009]. SWAN was developed originally by *Booij et al.* [1999] and improved by the SWAN Team [2006a; b]. Coupling of FVCOM and SWAVE was approached through the radiation stress, bottom boundary layer, and surface stress [*Wu et al.*, 2010; *Beardsley et al.*, 2013]. The wave-current bottom boundary layer (BBL) codes were developed by *Warner et al.* [2008] and converted into an unstructured-grid finite-volume version under the FVCOM framework.

The computational domain of GoM-FVCOM (called GoM3) covered the Scotian Shelf, Gulf of Maine (GoM) including the Bay of Fundy and Georges Bank, and the New England Shelf, and is enclosed by an open boundary running across the Delaware Shelf on the south, toward the northeast in the open boundary deeper than 2000 m and then across the Scotian Shelf on the north [*Sun et al.*, 2013].

2.3 NECOFS Hindcast

The NECOFS hindcast simulation project was started in 2010 to provide SeaPlan (http://www.seaplan.org/) and the Massachusetts Office of Coastal Zone Management (CZM) with a high-resolution NECOFS hindcast database for the years 1978-2010. The focus of the hindcast simulation was on the Gulf of Maine (including Massachusetts coastal waters). Up to the present, the NECOFS hindcast hourly fields cover the period from 1978 through 2013. The GoM-FVCOM was driven by the surface forcing output from MM5/WRF, freshwater discharges from 51 rivers, and tidal forcing at the open boundary constructed with eight tidal constituents (M_2,

S_2, N_2, K_2, K_1, P_1, O_1, and Q_1). These tidal constituents on the open boundary at the upstream part of the GoM and Georges Bank were tuned to get better tidal simulation, especially in the northern GoM and Bay of Fundy based on regional coastal and moored tidal measurements [*Chen et al.*, 2011]. Subtidal forcing at the open boundary was specified through one-way nesting with the Global-FVCOM [*Chen et al.*, 2014], which was run with assimilation of SST, SSH, and T/S profiles for the same period. The near-surface current output from NECOFS for 2000-2008 was used for the comparison with CODAR data in the Block Island Sound region.

2.4 Design of Process-oriented Model Experiments

To quantify the role of tidal rectification in the formation of permanent eddies observed in the CODAR data and predicted by NECOFS in the study region, we re-ran GoM-FVCOM for homogenous and stratified cases with only tidal forcing. To evaluate the impact of wave-current interaction on the near-surface current in this region, we selected Tropical Storm Barry that passed over Block Island Sound on June 4, 2007, and ran GoM-FVCOM with inclusion of surface waves. Barry developed from a low-pressure system in the southeastern Gulf of Mexico, moved rapidly northeastward with a speed of ~95 km/hr, and then became an extratropical cyclone on June 3. The Barry simulation covered the time period of May 20-June 10, 2007.

3. CODAR-NECOFS Comparisons

3.1 Tidal Currents and Kinetic Energy

The average water depth over the CODAR-covered area was 36.6 m and the corresponding average layer thickness of GoM-FVCOM was 0.81 m. In this region, the vertical profile was equally divided into 45 layers [*Sun et al.*, 2013], and the model water depth varied from 3 m to 65 m, corresponding to a layer thickness between 0.07-1.47 m. The model-computed near-surface velocity was located at the mid-depth of the first layer, so it varied in depth between 0.035-0.75 m. The CODAR measurement represents the averaged velocity from surface to the effective depth of ~0.5 m [*Stewart and Joy*, 1974]. In the CODAR study area, the vertical shear in the horizontal velocity was generally small, of order of 10^{-3} s^{-1} in the upper few meters. For this reason, the FVCOM-CODAR comparisons were made using the velocity in the first layer of GoM-FVCOM.

Kinetic energy spectra of the model-computed and observed time series were computed with a segment size of 2784 hours (116 days). Data gaps in CODAR were filled using UTide [*Codiga*, 2011]. The spectra were computed for the three-year continuous time series (December 2003 to December 2006) at four locations (Figure 2) selected for high data availability (greater than 60%) in continuous 'system on' period and representation of flow characteristics in different areas. Averaged over the four locations, the FVCOM and CODAR spectra were in good agreement at subtidal frequencies within a 95% confidence level, but the model over-predicted the energy level observed in CODAR at tidal frequencies (Figure 4). The differences in spectral density between

CODAR and FVCOM in the M_2, N_2, S_2, and K_1 frequencies were less than 80% of the 95% confidence range, except for O_1, which was 3% larger than the 95% confidence range. The current variability was dominated by the semidiurnal tides, which on average account for ~87 % of the total kinetic energy. The diurnal tides accounted for only ~4% with and the subtidal variability the remaining ~9% of the total kinetic energy.

While within the 95% confidence intervals, the model-computed kinetic energy density peaks tended to be higher at both semidiurnal and diurnal periods than the observed spectra. The model kinetic energy density between the diurnal and semidiurnal frequencies was also larger than the CODAR density.

The NECOFS was forced by the eight tidal constituents (M_2, N_2, S_2, K_2, O_1, P_1, K_1 and Q_1). The ellipse parameters of these eight constituents were calculated for the model and measurements over the period December 2003 to December 2006 using T_TIDE [*Pawlowicz et al.*, 2002]. In the Block Island Sound region, the M_2 tidal current was about a factor of five stronger than other semidiurnal and diurnal tidal constituents (Table 1). For the M_2 tidal current, the mean CODAR major axis (40.4 cm/s) was about 10% smaller than the model major axis (45.1 cm/s). The CODAR and model minor axis show the same tendency. The CODAR and model M_2 ellipse orientations and phases were quite similar, within ±5º and ±3º respectively. While the ratios of the CODAR and model major axes varied for the other constituents, the CODAR and model tidal ellipse orientations were similar for each constituent (Figure 5).

Letting Maj_{CODAR}, Maj_{model}, Min_{CODAR} and Min_{model} be the major and minor axis values of CODAR-derived and model-computed M_2 tidal currents, respectively, we defined the normalized major axis difference as the ratio of $|Maj_{model} - Maj_{CODAR}|$ to $0.5|\ Maj_{model} + Maj_{CODAR}|$, and the eccentricity difference as $Min_{model}/Maj_{model} - Min_{CODAR}/Maj_{CODAR}$. The normalized major axis difference was in a range of 0-0.3, with the largest value of ~0.3 occurring in western Block Island Sound (Figure 6a), where the CODAR measurement was on the line between Montauk Point and Misquamicut stations. The absolute eccentricity difference varied from 0 to 0.2, with the largest value over the inner shelf south of Long Island (Figure 6b). The absolute orientation difference was consistent with the normalized major axis difference (Figure 6a), which showed a large difference of up to 30° just west of Block Island (Figure 6c). The absolute phase difference also exhibited two sites with differences as large a 30° (Figure 6d). The mean and standard deviation (1σ) of the orientation and phase differences are 6.6° ± 5.0° and 9.0° ± 5.4° respectively.

The KE spectra (Figure 4), the tidal ellipse plots (Figure 5), and the discussion of the normalized major axis difference presented above all suggest that the model-computed tidal currents were larger than the CODAR-derived tidal currents. This difference can be estimated using the scatter plot comparisons of the CODAR and model M_2 tidal ellipse parameters shown in Figure 6e-h. The least-squared fit of $y=a+bx$ in Figure 6e yields a =-0.01 ± 0.02 and b =1.28 ± 0.04 (correlation squared = 0.96), indicating that NECOFS over predicts the M_2 tidal currents by about 28.0 % averaged over the study area.

3.2 Subtidal Currents

The CODAR-derived hourly surface currents were first low-pass filtered [*Beardsley and Rosenfeld*, 1983] and then used to compute daily, monthly, seasonal, and annual mean currents. The subtidal current comparison was made at the CODAR stations where and when long continuous time series are available (Figure 2, circled asterisk). The subtidal processing was based on a 33-hour low-passed filtering for the 6-hour sampled time series. NECOFS successfully reproduced the subtidal currents measured using CODAR in both u and v directions, with the mean (standard deviation) of the difference of 2.1 (8.3) cm/s and 3.5 (8.4) cm/s respectively (Figure 7).

The annual mean currents show a circulation pattern defined by several flows (Figure 8): eastward outflow of ~20 cm/s through the Race (Long Island Sound Outflow); southeastward flow in central Block Island Sound (Long Island Sound Outflow and Southwest Point Eddy); a permanent anticyclonic eddy-like current around the eastern tip of Long Island (Montauk Point Eddy), fed by the eastward outflow through the Race (Long Island Sound Outflow); and an eastward flow that bifurcated into northward and southward branches west of Block Island (Block Island Clockwise Circulation). The northward branch turned anti-cyclonically around the northern tip of Block Island (North Reef Eddy).

The model was consistent with the mean-flow pattern defined by CODAR, but without the data gaps provided a spatially more complete picture of flow connections with adjacent coastal regions (Figure 8). The model results suggested that the permanent southward flow over the inner

shelf east of Block Island was fed by two sources: an eastward flow from Block Island Sound and southward flow from the Rhode Island coast (Rhode Island Offshore Flow). The model also resolved a permanent large anti-cyclonic eddy between Fisher Island and Gardiners Island (Gardiners Island Eddy), and a small anticyclonic eddy on the northern tip of Block Island, which were only partially detected in the CODAR data.

The seasonally-averaged flow over the nine-year study period showed similar spatial patterns as the annual mean (Figure 9). The seasonal variability of this flow was closely related to the flow change in its upstream region of Rhode Island Sound. In spring and summer, the currents to the south of Block Island were southwestward, but in winter, they were southeastward. The model-predicted spatial scale of the anticyclonic eddy flow around the eastern tip of the Long Island was larger than that observed in the CODAR data. This was probably due to an uncertainty in the stratification simulation by GoM-FVCOM. A discussion will be given in the mechanism study section.

The monthly-averaged difference between the CODAR-derived and model-computed velocity at 334 sites was 6 cm/s or less in speed (model consistently biased positive) and 28º or less in direction over the time period from 2000 through 2008 (Figure 10). These errors were about the same order of the measurement standard errors estimated for the CODAR observations. The standard deviation of the differences at all 334 sites was in a range of 10 cm/s in speed and up to 45º in direction. The standard deviations were relatively larger than mean differences; we found that the big differences occurred mainly when the current speed was small (<10 cm/s) (Figure 11).

Large differences in direction (>30°) occurred less than 34% of the time.

Crosby et al. [1993] introduced a generalized method to compute vector correlations for use in oceanography and meteorology. Here we use this method to examine the correlation between the CODAR-derived and model-computed monthly-mean surface velocity vector time series. An extension of the standard one-dimensional correlation coefficient, this method for the two-dimensional vector computes the correlation coefficient squared ρ_v^2 which varies from 0.0 (no correlation when two samples are independent) to 2.0 (prefect correlation between two vector time series which are 100% dependent). It is important to note that the resulting value of ρ_v^2 is invariant under coordinate axes transformations, including rotations and changes in scale. In our case, the CODAR and model monthly vector time series have a total of 75 samples (Figure 10), so that $\rho_v^2 \leq 0.22$ indicates zero correlation at the 95% confidence level.

Figure 12 shows a color-coded map of the correlation coefficient squared (ρ_v^2). The correlation coefficient varied from a minimum of 0.21 to a maximum of 0.91 with a mean value of 0.51. The highest significant correlations were found associated with a) the Long Island Sound Outflow (the western region of BIS and in the northern inner shelf region) and b) the Block Island Clockwise Circulation (off the southern coast of Block Island). The vector correlations were below the zero correlation cutoff in approximately 0.6% of the area. We note that almost all of the CODAR and model vector time series exhibited some significant but limited (in comparison to ρ_v^2 = 2.0) correlation.

We also used the monthly-averaged velocities to calculate and compare monthly vorticity anomalies in the CODAR-derived and model-computed velocities in region A around the eastern tip of Long Island and in region B around Block Island (Figure 1), where the subtidal flow was anticyclonic. The model was capable of reproducing the seasonal and interannual variability of observed vorticity in these two regions (Figure 13). In region A, the observed vorticity anomaly showed a clear seasonal and interannual variability: strongest during summer as stratification increased and weakest during winter when there is less stratification; relatively weak during 2003-2005. This was also consistent with the fact that in summer the outflow from Block Island Sound turns anticyclonically to flow southwestward, while in winter, there were fewer tendencies for southwestward flow on the inner shelf; changes which were captured by the model. In region B, the temporal variability of the observed vorticity did not follow the same seasonal and interannual patterns shown in region A. The vorticity anomaly was dominated by negative values during 2001-2003 and by positive values during late-2005 to mid-2007. As the differences were within 10^{-4} s^{-1}, this interannual vortex variation pattern was also resolved in the model results (Figure 13).

3.3 Current-Wind Correlations

We estimated the correlation of winds and currents for the low-pass filtered CODAR and NECOFS hourly time series at six sites (Figure 1) selected as representative of different flow zones. Site 1 was in the Long Island Sound Outflow, site 2 was near the Rhode Island coast where the flow was influenced by the south- and westward along-shelf coastal flow from the upstream

region, site 3 was east of Block Island where the flow was southward, site 4 was south of Long Island in the permanent anticyclonic Montauk Point Eddy, site 5 was in the channel between the eastern tip of Long Island and Block Island, and site 6 was at ~40 m water depth over the mid-shelf.

The surface wind stress used in the correlation estimation was calculated using COARE3 [*Fairall et al.*, 2003] based on the MM5/WRF hindcast field of NECOFS with data assimilation of observed winds from all available coastal/shelf buoys. The horizontal resolution of the wind hindcast data was 9×9 km which were then interpolated to the six sites. The surface currents were highly correlated with the wind over the entire Block Island Sound with the correlation (0.4-1.0) much larger than the no correlation coefficient (0.1 at the 95% confidence level). In fall through winter, winds were from the northwest, while during late spring through summer, winds were predominately from the south or southwest (Figure 14). The seasonal mean wind stress was largest in winter and smallest in summer (Table 2). In all seasons, the wind stress variability as described by the principal axes was larger than the mean wind stress (Figure 15), with most (~73.5%) of the variance in the 2-10 day weather band and less than ~13.8% in the diurnal tidal and higher frequencies. These results were consistent with the study by *Lentz* [2008] and *O'Donnell et al.* [2014], which analyzed the long-term wind forcing observed from buoys, towers and coastal masts.

The time lagged correlations between the wind stress and the low-passed CODAR (maximum correlated wind directions shown with red arrows in Figure 16) and model hourly surface currents

(maximum correlated wind directions shown with blue arrows in Figure 16) were then computed as a function of the wind stress vector direction (with a one-hour time interval) and a *x*-*y* coordinate system aligned with the local along-isobath (green coordinates in Figure 16) at each site for the four (three-month) seasons. This process was conducted seasonally for the nine-year period 2000 through 2008 and maximum wind-current correlations in each season were averaged and are presented in Table 2 and Fig. 14.

At sites 1-6, the CODAR-derived and model-computed surface velocities were highly correlated with the surface wind stress (Table 2). For the along-isobath flow, the maximum wind-current correlation coefficients estimated for both measurement and model data ranged from 0.4 to 1.0, which were significantly higher than the critical value of 0.1 at a 95% confidence level. The differences in the correlation at the along-isobath direction were less than 37% for an average of the 6 sites (Table 2). The difference in the wind direction at the along-isobath direction at the maximum correlation for the CODAR and NECOFS data was less than 5º at sites 3 and 5; in a range of 15-35º at sites 1, 4, and 6; and up to 67º at site 2. The time lag at the maximum correlation ranged from 0-1.0 hours for the CODAR data and 0-4.5 hours for the NECOFS data. For the cross-isobath flow, the maximum current-wind correlations estimated for both measurement and model data was significantly higher than the critical value of 0.1 at a 95% confidence level, and the difference between measurement and model correlation was 0.2 or less. The differences in the wind direction and in the time lag at the maximum correlation for the CODAR and NECOFS data were in the range of 8-44° and 0-3 hours, respectively, similar to the results for the along-isobath

flow. Because of uncertainty in the current direction, perfect quantitative agreement in the current-wind correlation between CODAR and NECOFS flow fields was not expected. However, the consistent high correlation values found at these sites for the CODAR and NECOFS data suggested that the monthly variability of the surface current in the Block Island Sound was highly correlated to the change of the wind over seasons and years.

3.4 Influence of Wave-Current Interaction

The CODAR-NECOFS comparisons described above were made for the model results without the inclusion of wave-current interaction. *Chen et al.* [2013b] and *Beardsley et al.* [2013] examined the contribution of wave-current interaction to storm-induced coastal inundation. They reported that this interaction process could not only intensify the strength of the nearshore current but also alter its direction. While a relatively large difference between model-computed and CODAR-measured current direction may be due to measurement uncertainty, it was unclear if this was partially caused by the absence of the dynamics associated with wave-current interaction. For this reason, we re-ran the model with inclusion of wave-current interaction dynamics over the period during which the June 2007 extratropical storm Barry swept over Block Island Sound

The statistics of the data-model comparison for the cases with and without inclusion of wave-current interaction are summarized in Table 3. On June 4, 2007, Barry arrived in the Block Island Sound region at about 19:00 UTC and landed in South Kingstown, RI at 20:00 UTC. During the period between 19:00-24:00 UTC, the speed and direction differences averaged over the 334

sites between these two cases were in the range of 2-12 cm/s and 1-13°, and the mean differences in these 6 hours were 3 cm/s and 5º, which was within the CODAR measurement uncertainties (6 cm/s and 12º) during that period. The differences were only 50% and 42% of the CODAR measurement uncertainty in current speed magnitude and direction, respectively. This suggested that including wave-current interaction in the model simulation did not make a significant contribution to improving the accuracy of the model-CODAR comparison in this region.

4. ADCP-NECOFS Comparisons

Continuous moored ADCP measurements made near the southern entrance to Block Island Sound (Figure 1) between 2000 and 2002 [*Codiga and Houk*, 2002] are used here for further comparison with NECOFS model data. The ADCP 20-min data were screened using the following criteria: 1) the measurement period was longer than two months, and 2) the mooring location was within the 334 CODAR grid points used in this study. This resulted in seven ADCP time series from five sites (Table 4). Harmonic analysis using T_TIDE [*Pawlowicz et al.*, 2002] was then conducted on the vertically-averaged ADCP and NECOFS data.

The averaged ADCP and model tidal ellipse parameters for the three primary semidiurnal and two diurnal constituents (Table 5) show a small but clear tendency for the semidiurnal model-derived major axes to overestimate the ADCP major axes. This difference is most notable for the M_2 constituent, for which the mean difference is 1.9 ± 6.2 cm/s. The ADCP M_2 tidal ellipse parameters are plotted as red dots in the lower row in Figure 6. A least-squared fit of the seven

ADCP and model M_2 major axes using $y=a + b \times x$ in Figure 6e yields a = -0.04 ± 0.20 and b =1.07 ± 0.54, indicating no statistically significant difference. With an interpolation of the CODAR M_2 major axis to the ADCP locations, the difference between the ADCP and CODAR major axes is 2.8 ±1.8 cm/s.

The vertical tidal profiles computed using the ADCP data were also compared with NECOFS (Figure 17). The ADCP and NECOFS profiles match well, with the maximum differences less than 7.8 cm/s and 2.9 cm/s for major and minor axes respectively. The vertical averaged ADCP-NECOFS subtidal current difference for the seven ADCP stations is less than 5.0 cm/s.

Taken together, these results suggest that for the dominant M_2 component, NECOFS over predicts CODAR observations by ~28 % averaged over the study area. While there is a slight suggestion that the ADCP major axis is larger than the CODAR major axes, both ADCP and CODAR agree within the measurement uncertainties.

5. Mechanism Studies

A major finding from the CODAR and NECOFS comparisons was that despite seasonal and interannual changes in the wind, the subtidal flow pattern in Block Island Sound was nearly unchanged: eastward outflow through the Race; southeastward flow in Block Island Sound north of Long Island; and a permanent anticyclonic eddy-like current around the eastern tip of Long Island and around the northern tip of Block Island (Figure 8). To investigate the driving mechanism(s) for this stationary flow pattern and how it was influenced by the wind, we

conducted an EOF analysis based on the nine-year NECOFS vertically-averaged flow field. In order to study the whole pattern, the nine-year mean velocities were not subtracted from the total flow field.

Here we focus on the first two EOF modes, since they dominated the flow field in Block Island Sound and account for 89% and 7% of the total variance, respectively (Figure 18). The EOF analysis was based on the along-shelf direction defined as 36º counterclockwise from East based on the bathymetry in the outer Block Island Sound region.

EOF mode 1 represented the relatively stationary low-frequency flow pattern that was detected by CODAR and reproduced by NECOFS. The corresponding time series of the along- and cross-shelf velocity remained the same sign (all positive), so that this flow pattern is a permanent feature with a magnitude of 10-30 cm/s in this region. From an autocorrelation analysis of mode 1's temporal amplitude, the mode 1 period was one year. The mode 1 velocity varied with season: intensified during the summer and weaker during the winter.

EOF mode 2 was characterized mainly by the secondary cross-shelf flow and a relatively strong along-shelf flow. The corresponding time series of along- and cross-shelf velocity changed sign with season, suggesting that the cross-shelf flow was dominated by an offshore flow during late spring through summer and by an onshore flow during fall through winter. The amplitude of the mode 2 flow was in the order of ~1-2 cm/s. The nine-year flow field's velocity anomaly (i.e. with the mean removed) was also used to conduct a conventional complex EOF analysis. Mode 1

was largest, accounting for 68% of the total variance, and its pattern was nearly the same as mode 2 found in the previous EOF analysis (Figure 18 upper right panel).

It is clear that the wind was not the primary driving mechanism for the mode 1 flow since the wind changed direction with season. *Luo et al.* [2013] suggested the cyclonic flow around Rhode Island Sound was partially driven by tidal rectification. To test if mode 1 was caused by tidal rectification, we re-ran NECOFS with only tidal forcing under homogenous and summertime stratified conditions (Figure 19). The homogenous tidally-rectified flow pattern was similar to the mode 1 flow pattern (Figure 18: upper left panel): a strong cross-sound flow from the exit of Long Island Sound turned eastward around the northern coast of the eastern tip of Long Island; an anticyclonic eddy flow around the southern coast of the eastern tip of Long Island; multiflow separation eddies around the southern and northern tips of Block Island; combined southward flow from the northern coast of Rhode Island and eddy flow on the northern tip of Block Island produced an anticyclonic around-island flow over the eastern and southern shelves of Block Island. In the stratified case, the tidal-rectified flow pattern was similar but the magnitude of the velocity was intensified by a factor of up to 1.5 and the spatial scale of the anticyclonic eddy increased. These two experiments indicated that the relatively stationary flow pattern found in the EOF mode 1 was in part a result of tidal rectification, with intensification in summer due to stratification. A similar summer intensification of the tidal-rectified residual gyre over Georges Bank is described in *Chen et al.* [1995].

The model simulation results for homogenous and stratified cases clearly show that the

intensity and size of the anticyclonic eddy varied significantly with season as stratification changed. This could explain why the model-computed anticyclonic eddy had a relatively larger size than the CODAR-derived eddy shown in Figure 10; which could be a result of the uncertainty in the stratification simulation by the model.

We assume that the EOF mode 2 flow pattern was formed by the surface wind forcing with its direction changing with season. Southerly or southwesterly wind in summer pushed the water onshore and northwesterly wind in winter drained the water offshore. To demonstrate this, we calculated the correlation of the time series of the mode 2-constructed along- and cross-shelf velocity components with the surface wind stress. We found that the northward cross-shelf velocity showed a maximum correlation of 0.9 with the wind at a 90° angle. The critical value at a 95% confidence level was 0.1 based on the degree of freedom of the samples. This result suggests that the seasonal variation of the onshore and offshore water transport derived by the mode 2 velocity component was mainly driven by the wind following the Ekman transport theory. The eastward along-shelf velocity was also highly corrected with the wind. The maximum correlation coefficient was 0.8, but it occurred at a veering angle of ~130°. The correlation between the eastward velocity and northward wind stress was about 0.3. Although it was higher than a critical value of 0.1, it suggested that the along-shelf velocity derived by the mode 2 was not fully driven by the local wind-induced Ekman transport.

The correlation of the vertically average current with surface wind stress varied with season: highest in winter and slightly lower in summer. Examples are shown in Figure 20 for the

along-isobath and cross-isobath velocities at six selected sites. This result is consistent with the EOF analysis shown in Figure 18, which indicated that the seasonal variability of the flow field in this region was partially resulted from the stratified tidal rectification, which varied with season due to stratification. In winter, the water in the Block Island Sound was well mixed, so that the wind could play an essential role in the flow variability.

The current-wind correlation analysis suggested that the EOF mode 2 derived eastward along-shelf velocity did not comply with the wind-driven Ekman transport theory. We hypothesized that in addition to tidal rectification and wind, the flow variability in the Block Island Sound was also related to the change of the water transport into this region. To test this hypothesis, we estimated the correlation of the vertically averaged velocity and water transport between site 1 and section a, site 2 and section b, site 6 and section c (see Figure 1 for locations of the three sections). The results showed that the correlation was close to 1.0 between site 1 and section a, 0.8 between site 2 and section b, and 0.6 between site 6 and section c. All these values were significantly higher the critical value of 0.1 at the 95% confidence level. This result led us to believe that the flow variability in the Block Island Sound was also highly influenced by the flow change in its surrounding coastal and outer regions.

We next computed the long-term (9-year) monthly mean vector wind stress, temperature, salinity, and cross- and along-shelf currents at site 6 using NECOFS data (Figure 21). The water was stratified from May to October and vertically well-mixed in other months. The stratification was associated with the low salinity water advected from the Long Island Sound outflow [*Ullman*

and Codgia, 2004]. However, even when the water was completely mixed from winter to spring, the cross-shelf velocity had a clear two-layer circulation with offshore flow at the surface and onshore flow at the bottom. This structure was also observed by *Codiga* [2005]. Further analysis showed that the offshore net transport was accompanied with the presence of the onshore wind component. In turn, the onshore net transport co-occurred with the offshore wind component. This feature did not contradict the wind-driven Ekman theory found in the EOF analysis, where we found the cross-shelf water transport was highly correlated with the along-shelf wind stress. In summer, the southwesterly wind prevailed in Block Island Sound. The along-shelf wind stress was eastward, with an onshore cross-shelf wind stress component. The along-shelf wind-driven Ekman transport was offshore, which was accompanied with an onshore wind component. The reversed conclusion occurred in winter. This explained why cross-shelf net water transport was always in an opposite direction to the cross-shelf wind component.

6 Model limitations and future improvement

While the CODAR measurements contained an averaged hourly measurement uncertainty of 3-7 cm/s in speed and 4º-14º in direction, the fact from the CODAR- and ADCP-derived tidal velocity comparisons suggest that NECOFS overestimated the surface tidal velocity by ~28% in the Block Island Sound region. This difference could be related to the tidal forcing specified on the nesting boundary, local bathymetry, bottom roughness, and/or the vertical mixing.

Tidal forcing specified on the nesting boundary of GoM-FVCOM was from the inverse tidal

model developed by *Egbert et al.* [1994]. The tidal simulation results obtained in that model was based on the assimilation of tide gauge data with the minimum least square fitting error in the computational domain. Since the inverse tidal model did not accurately resolve the local bathymetry, the tidal elevation obtained from the inverse data assimilation was not accurate in the offshore region of the northeastern continental shelf. When GoM-FVCOM was initially developed, the tidal forcing on the northern side of the nesting boundary was adjusted to obtain the best tidal simulation results in the GoM/GB and Massachusetts coastal regions. However, there was no effort to adjust the tidal forcing along the southern side of the nesting boundary to improve the local tidal simulation. The resulting tidal simulation results were compared with all available sea level measurements at tidal gauges in the GoM/GB region [*Chen et al.* 2011]. *Chen et al.* [2011] pointed out that the tidal energy in the GoM/GB region originated from the North Atlantic Ocean, which entered the region through the Northeast Channel, while the tidal energy over the southern New England shelf was from the offshore open ocean region. Therefore, the adjustment made on the northern side of the nesting boundary would not improve the tidal simulation in the Block Island Sound region.

The GoM-FVCOM was initially configured with bathymetric data available in 1999. In 2013, J. O'Donnell and T. Fake (University of Connecticut) provided us with their high-resolution bathymetric dataset based on field surveys and LIDAR data obtained in Long Island Sound and a portion of the Block Island Sound region. We compared this new bathymetric data with the bathymetric database used in the old version of GoM-FVCOM and found in some regions the

difference between the newly surveyed and the model-used bathymetries could be up to ~10 m. While the bathymetry used in GoM-FVCOM for forecast operation has been improved with time, this improved bathymetry was not used in the NECOFS hindcast database used in this study.

Chen et al. [2011] examined the sensitivity of the tidal simulation to the parameterization in bottom roughness and vertical eddy viscosity in the GoM/GB region. By comparing with the observed bottom roughness, turbulent dissipation energy and vertical eddy viscosity, they found that the accuracy of tidal elevation and current simulation was sensitive to these parameters which must be specified in the model setup. The bottom roughness used in the GoM-FVCOM hindcast was based on model-data comparisons on GB and in the GoM [*Terray et al.*, 1996; 1997]. Since no comparison was made in the Block Island Sound region, the parameters specified in the GoM-FVCOM may not be suitable for this region. To evaluate how sensitive the tidal simulation in the study area is to these factors, we conducted the following experiments.

1) Boundary Tidal Forcing: we adjusted the M_2 tidal elevation on the southern side of the nesting boundary by a reduction of 5 cm and ran GoM-FVCOM for the case with only tidal forcing. The results showed that this tuning changed the M_2 tidal elevation at the Montauk station by a factor of less than 1 cm, which meant that the tidal elevation along the coast was sensitive to the setting of the tidal forcing on the nesting boundary by a response rate of 20%. However, the current version of GoM-FVCOM showed an underestimation of tidal elevation along the coast, and an overestimation of tidal current in the Block Island Sound region. Increasing the tidal elevation on the boundary will increase the amplitude of tidal currents and thus lead to a larger

error in the tidal current simulation. This analysis suggests that the error in the tidal current simulation was not caused by the setting of the tidal elevation on the nesting boundary.

2) Bathymetry: we re-ran the GoM-FVCOM with the updated bathymetry in the Long Island Sound and adjacent region for the case with only tidal forcing for a period of 3 months. In addition to an improvement in tidal elevation simulation along the coast, the average error in the M_2 tidal currents was reduced by a factor of 13% (Figure 22a), an improvement of ~46% compared with the model results used in the CODAR comparison. This suggests that the overestimation in the magnitude of the tidal currents in the Block Island Sound region was partially due to the inaccurate bathymetry used in the model.

To explore the effect of reduced tidal currents on tidal rectification (Figure 19), we reran the homogeneous case with the new bathymetry. The flow pattern was similar, but the strength of the residual current was reduced by about 5%.

3) Bottom Roughness: By increasing the bottom roughness value by a factor of four in the Block Island Sound region, we re-ran GoM-FVCOM for the case with only tidal forcing. The results showed that the overestimation of the M_2 values dropped by a factor of 16%, an improvement at a percent value of ~57% compared with the model results used in the CODAR comparison (Figure 22b). However, increasing the bottom roughness caused an underestimation of tidal elevation at coastal tidal gauges. Therefore, if the bottom roughness was an issue that caused the overestimation of tidal currents in Block Island Sound, it should vary in space. It is difficult to

accurately specify the spatially-varying bottom roughness parameter in the model without relevant direct measurements of bottom stress and/or bottom roughness taken in this region.

4) Vertical Eddy Viscosity: Although no experiment was made to test the sensitivity of the tidal simulation to vertical eddy viscosity, *Chen et al.* [1995] found that increased vertical mixing would increase the along-isobath rectified tidal currents, and vice versa.

The model-CODAR comparison results suggest that the tidal simulation in the Block Island Sound region needs to be improved. Preliminary experiments suggest that realistic changes to the tidal boundary conditions will not have a significant effect on the currents, but that improvements in local bathymetry and parameterization of bottom roughness will decrease the amplitude of the M_2 tidal current. The effects of changing vertical eddy viscosity remain to be explored.

7. Summary

A comparison was made between the global-regional nested FVCOM-produced and CODAR-derived surface currents for the period 2000 through 2008 in the Block Island Sound region. The model-computed and CODAR-derived kinetic energy spectrum densities matched at subtidal frequencies with the model slightly over predicting in the tidal frequencies within the 95% confidence interval. Both CODAR and model data indicated that the region was dominated by the semidiurnal tidal motion, which on average accounted for ~87% of the total kinetic energy. The subtidal variability accounted for ~9% and the diurnal tides the remaining ~4% of the total kinetic energy. Taking the CODAR averaged hourly uncertainty of 3-7 cm/s in speed and 4º-14º in

direction into account, the model reproduced the primary tidal flow pattern in this region.

The comparison of CODAR-derived and model-computed subtidal surface currents was made over daily to monthly time scales. The model-computed and CODAR-derived monthly averaged flow fields showed that over all four seasons, the flow field retained the same spatial distribution pattern: relatively strong southeastward outflow through the Race; a permanent anticyclonic eddy-like current around the southern area of the eastern tip of Long Island; and one around-island currents (BICC in Figure 8) that were separated on the western side of Block Island. High correlation coefficient values were found for the time series of CODAR-derived and model-computed surface velocities with the surface wind stress, suggesting that the monthly variability of the surface current in the Block Island Sound region was highly correlated to the change in the wind stress over seasons and years.

The June 2007 extratropical storm Barry was selected to estimate the impact of wave-current interaction dynamics on the model-CODAR comparison. The statistics of the CODAR-model comparison for the cases with and without inclusion of wave-current interaction suggested that including wave-current interaction processes in the model simulation did not significantly improve the accuracy of the model-CODAR comparison in this region.

EOF analysis results showed that the subtidal low-frequency flow field in the Block Island Sound region was strongly controlled by the first and second modes, which accounted for 89% and 7% of the total variance, respectively. Mode 1 represented the relatively stationary low-frequency

flow pattern that was detected by the CODAR and model. The corresponding time series of cross- and along-shelf velocity remained the same sign, so that this flow pattern is a permanent feature, with its magnitude intensifying during the summer and weakening during the winter. Mode 2 was characterized mainly by the secondary cross-shelf flow and a strong along-shelf flow. The corresponding time series showed the cross-shelf velocity changed direction with season: the cross-shelf flow was dominated by an onshore flow during late spring through summer and by an offshore flow during fall through winter.

The process-oriented model experiments indicated that the relatively stationary flow pattern found in mode 1 was a result of tidal rectification and the seasonal variability was caused by stratified tidal rectification that was strongest during summer as stratification developed and weakest during the winter when the water is vertically well mixed. Correlation analysis between the flow and wind stress suggested that the mode 2 flow pattern was formed by the surface wind forcing with its direction changing with season. The mode 2 onshore and offshore water transport complied with wind-driven Ekman theory, while the along-shelf water transport was driven not only by the surface wind stress but was also influenced by the water transport from the surrounding coastal and shelf regions.

Acknowledgments

This work was supported by the NSF grants OCE-1332207 and OCE-1332666, MIT Sea Grant College Program through grant 2012-R/RC-127, and the NOAA NERACOOS program funds for NECOFS. Operational funding for the CODAR systems used in this study was provided by the Mid-Atlantic Regional Association Coastal Ocean Observing System. The development of the Global-FVCOM system has been supported by NSF grants OCE-1203393. C. Chen's contribution was also supported by the International Center for Marine Studies at Shanghai Ocean University through the "Shanghai Universities First-class Disciplines Project". We would like to thank Dan Codiga and James O'Donnell for the ADCP data, Todd Fake for the operation and maintenance of these CODAR systems, Miles Sundermeyer for helpful discussions and Zhigang Lai for providing the Global-FVCOM output for the nesting boundary conditions. James O'Donnell and Bruce Taggart provided helpful reviews and suggestions. Any use of trade, firm, or product names is for descriptive purposes only and does not imply endorsement by the U.S. Government.

References

Barrick D.E. (2008a), 30 years of CMTC and CODAR. Proceeding IEEE OES Ninth Working *Conference on Current Measurement Technology*, 131-136, March 17-19, New York: IEEE.

Barrick, D.E., C.C. Teague and P.M. Lilleboe (2008b), Systems and methods for monitoring river flow parameters using a VHF/UHF radar station, U.S. Patent Application 20090195437.

Beardsley, R.C., and L. K. Rosenfeld (1983), Introduction to the CODE-1 moored array and large-scale data report, in CODE-1: Moored Array and Large-Scale Data Report, edited by L. K. Rosenfeld, Woods Hole Oceanography Institute Technical Report WHOI-83-23, CODE Technical Report 21, Woods Hole, MA, 1216 pp.

Beardsley, R.C., and W.C. Boicourt (1981), On estuarine and continental-shelf circulation in the Middle Atlantic Bight, *Evolution of Physical Oceanography*, B. A. Warren and C. Wunsch, eds., MIT Press, Cambridge, Mass., 198-233.

Beardsley, R.C., C. Chen and Q. Xu (2013), Coastal flooding in Scituate (MA): a FVCOM study of the December 27 2010 nor'easter*, Journal of Geophysical Research*, 118, 6030–6045, doi:10.1002/2013JC008862.

Blumberg, A.F., and B. Galperin (1990), On the summer circulation in New York Bight and contiguous estuarine waters, *Coastal and estuarine studies*, 38, Residual currents and long-term transport, 451-467, doi: 10.1029/CE038p0451.

Blumberg, A.F., and D.W. Prichard (1997), Estimates of the transport through the East River, New York, *Journal of Geophysical Research*, 102(3), 5685-5703, doi: 10.1029/96JC03416.

Booij, N., R.C. Ris and L.H. Holthuijsen (1999), A third-generation wave model for coastal regions, Part I, Model description and validation, *Journal of Geophysical Research, 104*, C4, 7649-7666, doi: 10.1029/98JC02622.

Burchard, H. (2002), Applied turbulence modeling in marine waters, *Lecture Notes in Earth Sciences 100*, 215, Springer-Verlag, Berlin, Germany.

Chao, Y., Z. Li, J. Farrara, J.C. McWilliams, J. Bellingham, X. Capet, F. Chavez, J.K. Choi, R. Davis, J. Doyle, D.M. Fratantoni, P. Li, P. Marchesiello, M.A. Moline, J. Paduan, S. Ramp (2009), Development, implementation and evaluation of a data-assimilative ocean forecasting system off the central California coast, *Studies in Deep-Sea Research Part II-Topical Oceanography*, 56(3-5), 100-126, doi: 10.1016/j.dsr2.2008.08.011.

Chen, C., R.C. Beardsley, and R. Limeburner (1995), A numerical study of stratified tidal rectification over finite-amplitude banks, part II: Georges Bank. *Journal of Physical Oceanography*, 25, 2111-2128.

Chen, C., H. Liu, and R.C. Beardsley (2003), An unstructured grid, finite-volume, three-dimensional, primitive equations ocean model: Application to coastal ocean and estuaries, *Journal of Atmospheric and Oceanic Technology*, 20(1), 159-186, doi: 10.1175/1520-0426(2003)020.

Chen, C., R.C. Beardsley, S. Hu, Q. Xu, and H. Lin (2005), Using MM5 to hindcast the ocean surface forcing fields over the Gulf of Maine and Georges Bank region, *Journal of Atmospheric and Oceanic Technology,* 22 (2), 131-145, doi: 10.1175/JTECH-1682.1.

Chen, C., R.C. Beardsley, and G. Cowles (2006), An unstructured grid, finite-volume coastal ocean model (FVCOM) system, *Oceanography,* 19*,* 78-89, doi: 10.5670/oceanog.2006.92.

Chen, C., H. Huang, R. C. Beardsley, Q. Xu, R. Limeburner, G. W Cowles, Y. Sun, J. Qi and H. Lin (2011), Tidal dynamics in the Gulf of Maine and New England Shelf: An application of FVCOM, *Journal of Geophysical Research*, 116, C12010, doi: 10.1029/2011JC007054.

Chen, C., R.C. Beardsley, G. Cowles, J. Qi, Z. Lai, G. Gao, D. Stuebe, Q. Xu, P. Xue, J. Ge, R. Ji, S. Hu, R. Tian, H. Huang, L. Wu, H. Lin, Y. Sun and L. Zhao (2013a), An unstructured grid, finite-volume community ocean model FVCOM user manual, SMAST/UMASSD Technical Report 13-0701, School of Marine Science and Technology, University of Massachusetts-Dartmouth, New Bedford, MA

Chen, C., R.C. Beardsley, R.A Luettich Jr, J.J. Westerink, H. Wang, W. Perrie, Q. Xu, A.S. Dohahue, J. Qi, H. Lin, L. Zhao, P. Kerr, Y. Meng and B. Toulany (2013b), IOOS/SURA Extratropical Storm Inundation Testbed: Inter-model (ADCIRC, FVCOM and SELFE) comparisons in Scituate, Massachusetts, *Journal of Geophysical Research*, 118, doi: 10.1002/jgrc.20397.

Crosby, D.S., L.C. Breaker, and W.H. Gemmill (1993), A proposed definition for vector correlation in geophysics: Theory and application, *Journal of Atmospheric Oceanic Technology*, 10, 355-367, doi: 10.1175/1520-0426.

Codiga, D.L. and A.E. Houk (2002), Current profile time series from the FRONT moored array, Technical Report, Department of Marine Sciences, University of Connecticut, Avery Point, CT, 19 pp.

Codiga, D.L. (2005), Interplay of wind forcing and buoyant discharge off Montauk Point: Seasonal changes in velocity structure and a coastal front, *Journal of Physical Oceanography*, 35(6), 1068–1085, doi: 10.1175/JPO2736.1.

Codiga, D.L. (2011), Unified tidal analysis and prediction using the UTide Matlab functions, Technical Report 2011-01, Graduate School of Oceanography, University of Rhode Island, Narragansett, RI, 59 pp.

Dong, C.M., E.Y. Idica, and J.C. McWilliams (2009), Circulation and multiple-scale variability in the Southern California Bight, *Progress in Oceanography*, 82(3), 168-190, doi: 10.1016/j.pocean.2009.07.005.

Dudhia, J., and J.F. Bresch (2002), A global version of the PSU-NCAR Mesoscale Model, *Monthly Weather Review,* 130(12), 2989-3007, doi: 10.1175/1520-0493(2002)130.

Edwards, C.A., T.A. Fake, and P.S. Bogden (2004), Spring-summer frontogenesis at the mouth of Block Island Sound: 1. A numerical investigation into tidal and buoyancy-forced motion, *Journal of Geophysical Research,* 109, C12021, doi: 10.1029/2003JC002132.

Egbert G.D., A.F. Bennett Michael G.G. Foreman (1994), TOPEX/POSEIDON tides estimated using a global inverse model, *Journal of Geophysical Research*, 99(12), 24821-24852, doi: 10.1029/94JC01894.

Fairall, C.W., E.F. Bradley, J.E. Hare, A.A. Grachev, and J.B. Edson (2003), Bulk parameterization of air-sea fluxes: updates and verification for the COARE algorithm, *Journal of Climate*, 16, 571-591, doi: 10.1175/1520-0442(2003)016.

Graber, H.C., B.K. Haus, R.D. Chapman, and L.K. Shay (1997), HF radar comparisons with moored estimates of current speed and direction: Expected differences and implications, *Journal of Geophysical Research*, 102(C8), 18749-18766, doi: 10.1029/97jc01190.

Holman, R., and M.C. Haller (2013), Remote Sensing of the Nearshore, *Annual Review of Marine Science*, 5(5), 95-113, doi: 10.1146/annurev-marine-121211-172408.

Hopkins, T.S., and D.A. Dieterle (1983), An externally forced barotropic circulation model for the New York Bight, *Continental Shelf Research*, 2, 49-73, doi: 10.1016/0278-4343(83)90022-5.

Hopkins, T.S., and D.A. Dieterle (1987), Analysis of the baroclinic circulation of the New York Bight with a 3-D diagnostic model, *Continental Shelf Research*, 7, 237–265, doi: 10.1016/0278-4343(87)90068-9.

Hubbard, M.E. (1999), Multidimensional slope limiters for MUSCL type finite volume schemes on unstructured grids, *Journal of Computational Physics*, 155, 54-74, doi: 10.1006/jcph.1999.6329.

Ianniello, J.P. (1981), Tidally-induced residual currents in Long Island and Block Island Sounds, *Estuarine Coastal and Shelf Science*, 12, 177-191, doi: 10.1016/S0302-3524(81)80095-3.

Kim, S.Y., E.J. Terrill, B.D. Cornuelle, B. Jones, L. Washburn, M.A. Moline, J.D. Paduan, N. Garfield, J.L. Largier, G. Crawford, and P. M. Kosro (2011), Mapping the U.S. West Coast surface circulation: A multiyear analysis of high-frequency radar observations, *Journal of Geophysical Research*, 116, doi: 10.1029/2010jc006669.

Kobayashi, M.H., J.M.C. Pereira, and J.C.F. Pereira (1999), A conservative finite-volume second-order-accurate projection method on hybrid unstructured grids, *Journal of Computational Physics*, 150, 40-45, doi: 10.1006/jcph.1998.6163.

Kundu, P.K. (1976a), Ekman veering observed near the ocean bottom. *Journal of Physical Oceanography*, 6, 238-242, doi: 10.1175/1520-0485(1976)006<0238.

Kundu, P.K. and J.S. Allen (1976b), Some three-dimensional characteristics of low-frequency current fluctuations near the Oregon coast, *Journal of Physical Oceanography*, 6:181-199, doi: 10.1175/1520-0485(1976)006<0181.

Lentz, S.J. (2008), Seasonal variations in the circulation over the Middle Atlantic Bight continental shelf, Journal of Physical Oceanography, 38:1486–1500, doi: 10.1175/2007JPO3767.1

Lipa, B.J. and D.E. Barrick (1983), Least-squares methods for the extraction of surface currents from CODAR crossed-loop data: Application at ARSLOE, *IEEE Journal of Oceanic Engineering,* OE-8*,* 226-253.

Liu, Y., R.H. Weisberg, and C.R. Merz, (2014) Assessment of CODAR SeaSonde and WERA HF Radars in Mapping Surface Currents on the West Florida Shelf, *Journal of Atmospheric and Oceanic Technology*, 31, 1363–1382, doi: 10.1175/JTECH-D-13-00107.1.

Luo, Y., L. Rothstein, Q. Liu, and S. Zhang (2013), Climatic variability of the circulation in the Rhode Island Sound: A modeling study, *Journal of Geophysical Research*, 118, 4072–4091, doi: 10.1002/jgrc.20285.

Mau, J.C., D.P. Wang, D.S. Ullman, and D.L. Codiga (2008), Model of the Long Island Sound outflow: Comparison with year-long HF radar and Doppler current observations, *Continental Shelf Research*, 28, 1791-1799, doi: 10.1016/j.csr.2008.04.013.

North, G.R., T.L. Thomas, R.F. Cahalan, and F.J. Moeng (1982), Sampling errors in the estimation of Empirical Orthogonal Functions, *Monthly Weather Review*, 110: 699-705, doi: 10.1175/1520-0493(1982)110.

O'Donnell, J., D. Ullman, M. Spaulding, E. Howlett, T. Fake, P. Hall, T. Isaji, C. Edwards, E. Anderson, T. McClay, J. Kohut, A. Allen, S. Lester, C. Turner, and M. Lewandowski (2005), Integration of coastal ocean dynamics application radar (CODAR) and short-term prediction system(STPS) surface current estimates into the Search and Rescue Optimal Planning System (SAROPS). U.S. Coast Guard Techical Report, CG-D-01-2006.

O'Donnell, J., R.E. Wilson, K. Lwiza, M. Whitney, W.F. Bohlen, D. Codiga, D.B. Fribance, T. Fake, M. Bowman, and J. Varekamp (2014), The Physical Oceanography of Long Island

Sound. In Long Island Sound: Prospects for the Urban Sea. Latimer, J.S., Tedesco, M., Swanson, R.L., Yarish, C., Stacey, P., Garza, C. (Eds.), ISBN-13: 978-1461461258.

Paduan, J.D., and L. Washburn (2013), High-Frequency Radar Observations of Ocean Surface Currents, *Annual Review of Marine Science*, 5, 115-136, doi: 10.1146/annurev-marine-121211-172315.

Pawlowicz, R., R. Beardsley, and S. Lentz (2002), Classical tidal harmonic analysis including error estimates in MATLAB using T_TIDE, *Computers and Geosciences*, 28, 929-937, doi: 10.1016/S0098-3004(02)00013-4.

Qi, J., C. Chen, R.C. Beardsley, W. Perrie, G.W. Cowles, and Z. Lai (2009), An unstructured-grid finite-volume surface wave model (FVCOM-SWAVE): Implementation, validations and applications, *Ocean Modeling*, 28(1-3), 153-166, doi: 10.1016/j.ocemod.2009.01.007.

Scheffner, N.W., S.R. Vermulakonda, D.J. Mark, H.L. Butler, and K.W. Kim (1994), *New York Bight study. Report 1: Hydrodynamic modeling,* Technical Report CERC-94-4, U.S. Army Corps of Engineers, Vicksburg, MS.

Shulman, I., C.R. Wu, J.K. Lewis, J.D. Paduan, L.K. Rosenfeld, J.C. Kindle, S.R. Ramp, and C.A. Collins (2002), High resolution modeling and data assimilation in the Monterey Bay area, *Continental Shelf Research*, 22(8), 1129-1151, doi: 10.1016/s0278-4343(01)00100-5.

Shulman, I., J. Kindle, P. Martin, S. Derada, J. Doyle, B. Penta, S. Anderson, F. Chavez, J. Paduan, and S. Ramp (2007), Modeling of upwelling/relaxation events with the Navy

Coastal Ocean Model, *Journal of Geophysical Research*, 112(C6), doi: 10.1029/2006jc003946.

Skamarock, W.C., and J.B. Klemp (2008), A time-split nonhydrostatic atmospheric model for research and NWP applications, *Journal of Computational Physics*, special issue on environmental modeling, 227(7), 3465-3485, doi: 10.1016/j.jcp.2007.01.037.

Salstein D.A., R.D. Rosen, and J.P. Peixoto (1983), Modes of variability in annual hemispheric water vapor and transport fields, *Journal of the Atmospheric Science*, 40:788-802, doi: 10.1175/1520-0469(1983)040<0788.

Stewart, R.H., and J.W. Joy (1974), HF radio measurements of surface currents, *Deep-Sea Research*, 21(12), 1039-1049, doi: 10.1016/0011-7471(74)90066-7.

Smagorinsky, J. (1963), General circulation experiments with the primitive equations, *Monthly Weather Review*, 91, 99-164, doi: 10.1175/1520-0493(1963)091.

Sun Y., C. Chen, R.C. Beardsley, Q. Xu, J. Qi, and H. Lin (2013), Impact of Current-Wave Interaction on Storm Surge Simulation: A Case Study for Hurricane Bob, *Journal of Geophysical Research*, 118, 2685-2701, doi: 10.1002/jgrc.20207.

SWAN Team (2006a), SWAN Cycle III version 40.51 Technical documentation, Delft University of Technology, Faculty of Civil Engineering and Geosciences, Environmental Fluid Mechanics Section, 2600 GA Delft, The Netherlands, 105 pp.

SWAN Team (2006b), SWAN Cycle III version 40.51 user manual. Delft University of Technology, Faculty of Civil Engineering and Geosciences, Environmental Fluid Mechanics Section, 2600 GA Delft, The Netherlands.

Terray, E.A., M.A. Donelan, Y.C. Agrawal, W.M. Drennan, K.K. Kahma, A.J. Williams, P.A. Hwang, and S.A. Kitaigorodskii (1996), Estimates of Kinetic Energy Dissipation under Breaking Waves, *Journal of Physical Oceanography*, 26, 792-807, doi: 10.1175/1520-0485(1996)026<0792.

Terray, E.A., M.A. Donelan, Y.C. Agrawal, W.M. Drennan, K.K. Kahma, A.J. Williams, P.A. Hwang, and S.A. Kitaigorodskii (1997), Estimates of Kinetic Energy Dissipation under Breaking Waves-Reply, *Journal of Physical Oceanography*,27, 2308-2309.

Thiebaux H.J., F.W. Zwiers (1984), The interpretation and estimation of effective sample size, *Journal of Climate and Applied Meteorology*, 23:800-811, doi: 10.1175/1520-0450(1984)023<0800.

Ullman, D.S., and D.L. Codiga (2004), Seasonal Variation of a Coastal Jet in the Long Island Sound Outflow Region Based on HF Radar and Doppler Current Observations*, Journal of Geophysical Research,* 109, C7, doi: 10.1029/2002JC001660.

Warner, J.C., S.R. Christopher, and S.P. Richard (2008), Development of a three-dimensional, regional, coupled wave, current, and sediment-transport model, *Computers and Geosciences*, 34(10), 1284-1306, doi: 10.1016/j.cageo.2008.02.012.

Wu, L, C. Chen, F. Guo, M. Shi, J. Qi, and J. Ge (2010), A FVCOM-based unstructured grid wave, current, sediment transport model, I. model description and validation, *Journal of Ocean University of China*, 10(1), 1-8, doi: 10.1007/s11802-011-1788-3.

Table

Table 1: Statistics of CODAR-derived and model-computed tidal ellipse parameters averaged over 334 sites. For each parameter, the mean and standard deviation are listed. The ellipse orientation is counterclockwise relative to E.

Tidal constituents	Major axis (cm/s) Mean ± Std		Minor axis (cm/s) Mean ± Std		Ellipse orientation (º) Mean ± Std		Phase (º) Mean ± Std	
	CODAR	NECOFS	CODAR	NECOFS	CODAR	NECOFS	CODAR	NECOFS
M_2	40.4±20.0	45.1±27.0	6.4±3.5	6.8±3.6	110.5±43.6	101.2±44.7	26.8±20.5	32.3±20.5
S_2	7.0±3.6	8.9±5.5	0.9±0.6	1.1±0.8	107.1±45.0	101.9±44.9	35.6±19.1	36.8±20.3
N_2	8.5±4.0	9.6±5.4	1.3±0.6	1.5±0.7	101.5±44.7	99.7±44.0	60.0±75.2	64.1±73.9
K_2	1.5±0.8	0.5±0.3	0.2±0.2	0.0±0.1	103.6±47.7	94.3±45.4	32.3±26.0	15.3±18.4
K_1	4.0±0.8	5.3±1.1	2.0±0.8	1.8±0.9	94.4±63.0	157.3±43.9	58.2±38.7	45.9±18.7
P_1	1.6±0.5	1.2±0.4	0.8±0.4	0.9±0.4	85.0±31.5	92.1±55.0	88.0±61.8	75.0±62.5
O_1	3.2±0.8	4.0±1.6	0.5±0.5	0.8±0.8	81.3±48.0	77.9±46.2	143.4±18.1	145.5±22.1
Q_1	0.7±0.2	0.6±0.2	0.2±0.2	0.2±0.1	93.2±48.3	85.6±48.1	120.4±29.2	110.3±30.7

Table 2: The maximum correlation between wind and along-isobath and cross-isobath current estimated for CODAR and NECOFS data (see Figure 1 for site locations). The cross-isobath direction is 90º counterclockwise from the along-isobath direction. C is the maximum correlation value; D is the difference (in degrees) in wind direction from the along- or across-isobath direction at the maximum correlation; and T is the time lag in hours at the maximum correlation. The inertial period in BIS is ~18 hours.

Site	Along-isobath						Cross-isobath					
	CODAR			NECOFS			CODAR			NECOFS		
	C	D	T	C	D	T	C	D	T	C	D	T
1	0.6	10	1.0	0.8	33	0.6	0.6	104	0.0	0.8	136	1.4
2	0.6	13	0.8	0.8	80	0.7	0.7	105	0.1	0.8	149	0.0
3	0.9	53	0.0	0.9	51	0.0	0.9	142	0.0	0.8	134	0.0
4	0.8	24	0.1	0.8	39	1.8	0.5	112	0.0	0.4	93	3.4
5	0.6	-64	1.6	0.5	-65	3.1	0.8	19	0.2	0.9	44	2.1
6	0.7	23	0.3	0.8	58	4.5	0.7	113	0.4	0.7	147	0.0

Table 3: Statistics of NECOFS and CODAR data comparisons on June 4, 2007, for the cases with and without the inclusion of wave-current interaction. The speed/direction differences were the difference between CODAR and model (with or without wave cases) in speed magnitude/ vector direction; the CODAR speed/direction errors were the measurement uncertainty at that hour.

Time (UT) (hour: m in)	Speed difference (cm/s)		CODAR speed Errors (cm/s)	Direction difference (º)		CODAR direction Errors (º)
	No wave	With wave		No wave	With wave	
19:00	15	23	5	21	29	14
20:00	20	25	6	3	8	12
21:00	27	25	6	-5	-4	12
22:00	24	16	6	-20	-14	11
23:00	18	6	6	-19	-10	10
24:00	12	2	5	-17	-4	12
Mean	19	16	6	-6	1	12
RMS	6	10	1	16	16	1

Table 4: ADCP record name, location, top and bottom bins of the instrument observation, water depth, start time and end time. Note that the FA01-N and SP02-Nm records were collected at the same site at different times. The FA01-W and SP02-Wm records were also collected at another site at different times. Thus, only five ADCP sites are shown in Figure 1.

ID	Name	Longitude (ºW)	Latitude (ºN)	Top Bin (m)	Bottom Bin (m)	Water Depth (m)	Start time	End time
1	FA01-N	71.75	41.06	1.78	12.28	14.61	02-Oct-2001	15-Jan-2002
2	FA01-W	71.79	41.00	3.07	30.57	32.91	05-Sep-2001	10-Mar-2002
3	SP01-Wm	71.79	40.98	2.89	32.33	34.21	14-Mar-2001	03-Jun-2001
4	SP02-Nm	71.75	41.06	2.06	12.06	14.31	21-Mar-2002	04-Jun-2002
5	SP02-Wm	71.79	41.00	3.31	30.81	32.56	21-Mar-2002	03-Jun-2002
6	WI01-E	71.68	40.98	3.01	38.85	41.61	19-Dec-2000	22-Feb-2001
7	WI01-W	71.74	40.99	3.57	43.07	44.76	19-Dec-2000	22-Feb-2001

Table 5: ADCP-derived and NECOFS-computed tidal ellipse parameters averaged over seven records at the five sites (Table 4). In this analysis, the ADCP and model currents were averaged in the vertical to provide the best estimate of the barotropic tidal current.

Tidal constituents	Major axis (cm/s) Mean ± Std.		Minor axis (cm/s) Mean ± Std.		Ellipse orientation (º) Mean ± Std.		Phase (º) Mean ± Std.	
	ADCP	NECOFS	ADCP	NECOFS	ADCP	NECOFS	ADCP	NECOFS
M_2	32.8±1.6	34.7±1.0	8.2±2.1	8.3±2.1	81.5±13.9	80.5±11.6	30.0±12.3	24.5±1.3
S_2	5.5±2.8	6.6±2.9	1.3±0.3	1.6±0.2	81.5±14.7	76.9±13.6	36.1±24.9	27.9±4.7
N_2	7.6±3.3	7.7±2.7	2.0±0.5	1.9±0.3	77.6±13.3	77.9±11.4	107.0±60.3	126.4±84.1
K_1	4.2±0.5	4.0±0.7	1.3±1.1	0.7±0.7	62.3±57.3	37.9±62.4	51.5±39.8	48.5±20.9
O_1	4.1±1.0	5.4±0.7	0.6±0.4	0.5±0.2	48.3±19.8	46.5±14.7	140.0±14.7	143.0±15.1

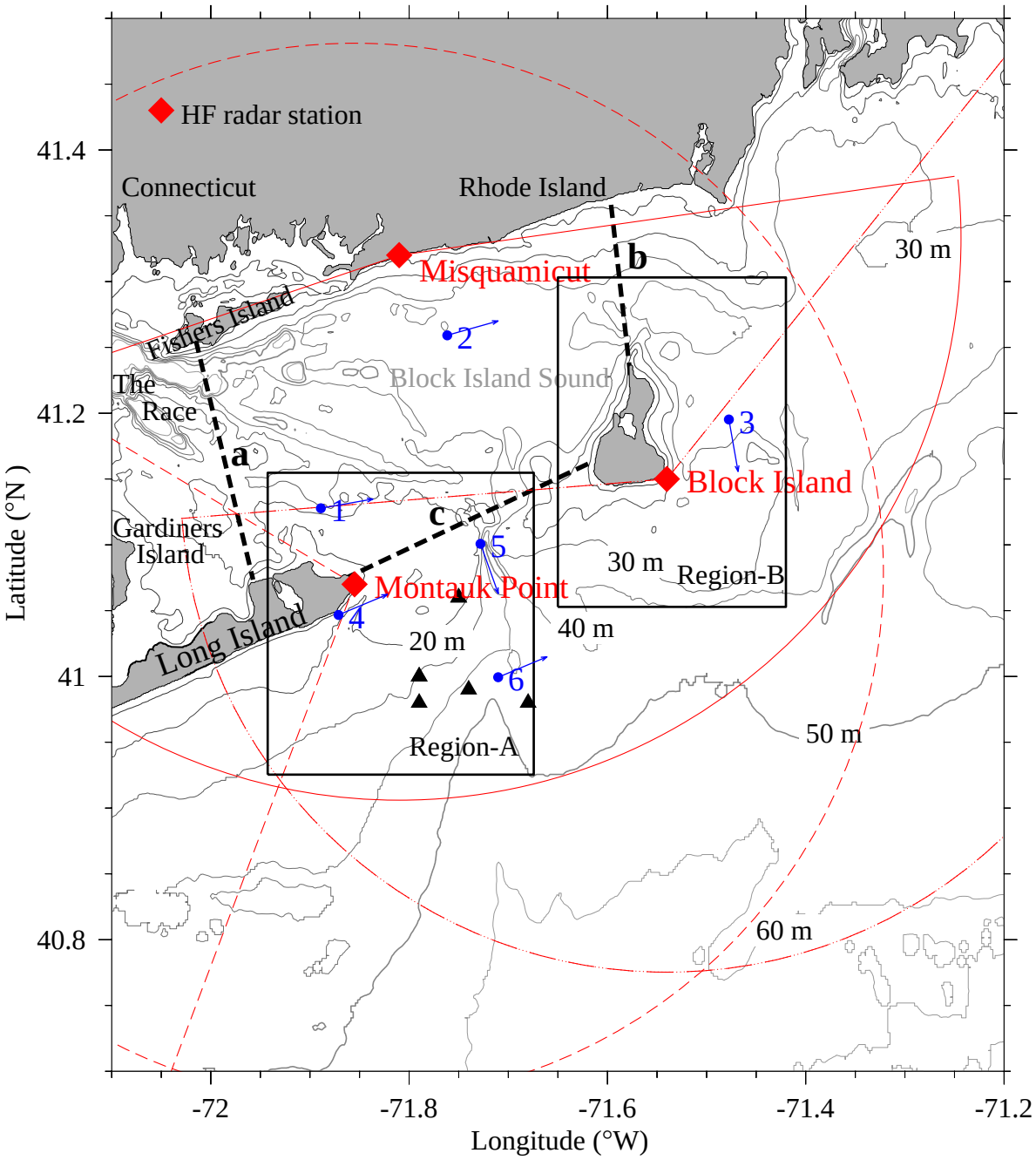

Figure 1. The locations of three high frequency (HF) coastal ocean dynamics application radars (CODAR) stations at Montauk Point, Misquamicut and Block Island (red diamonds) and their nominal coverage areas (marked by red sectors). The black triangles indicate the ADCP locations. The blue dots indicate the locations of the six sites numbered 1-6 that were selected for the current-wind correlation analysis. The blue arrows show the along-isobath direction used to define the velocity components at these sites (cross-isobath is 90° counterclockwise from this direction). Dashed black lines are transects a, b, and c where the water cross-transect transports were calculated. The boxes labeled Region-A and Region-B are the areas where model-computed and CODAR-derived vorticities were compared.

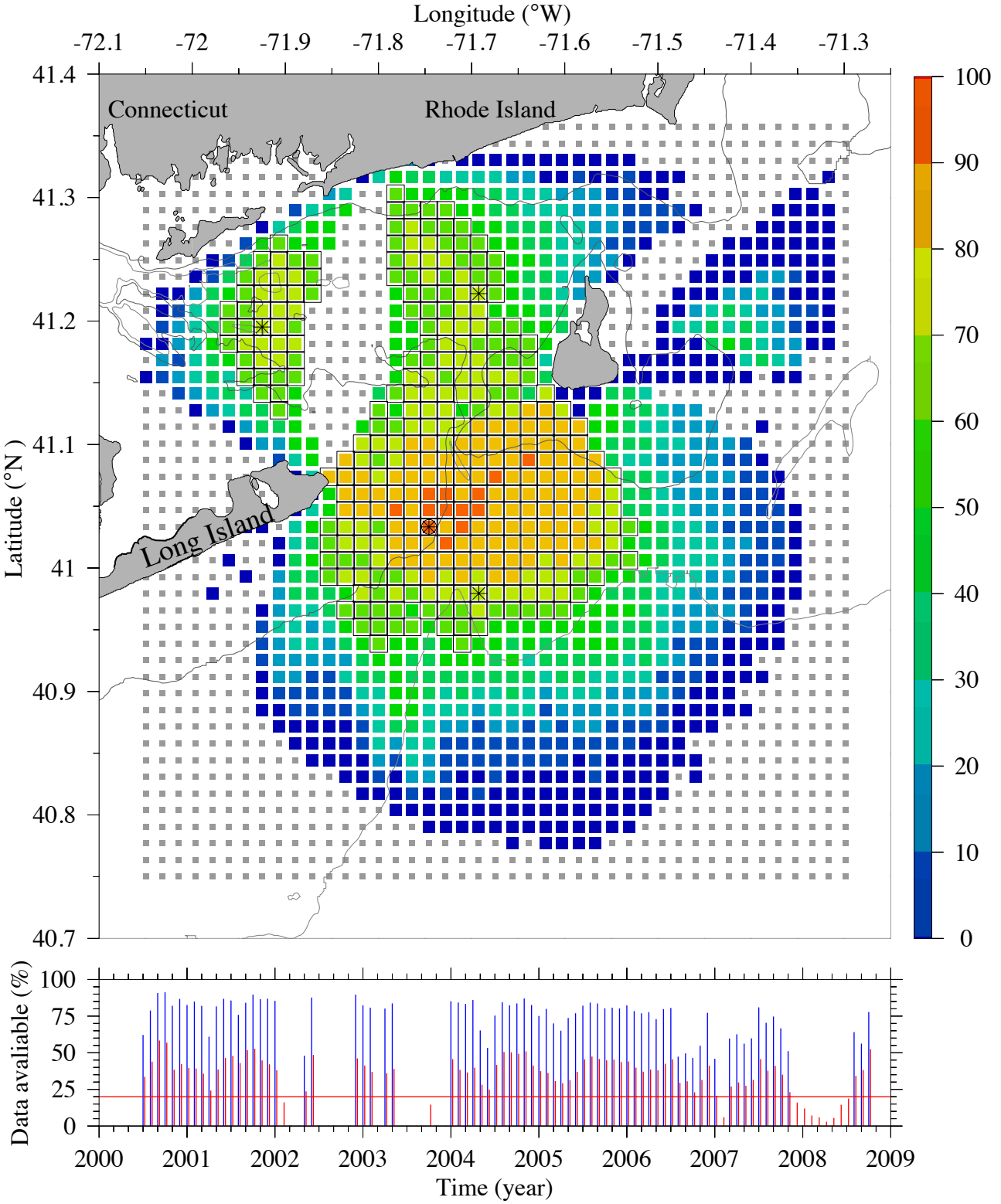

Figure 2. The gridded CODAR data locations for a 46×43 grid. In the upper panel, the colored squares show the percentage of the data availabile in each grid cell, the grey squares show no data available. The 334 sites with data availability greater than 60% and used for analysis are outlined in black. The black asterisks mark the four locations selected for the spectral analysis. The lower panel shows the percentage of hourly data availabile in each month; the blue vertical lines are for the 334 grid points, and the red vertical lines are for the 1147 grid points with data, and the red horizontal line at 20% is the lower limit for 'system on' monthly data.

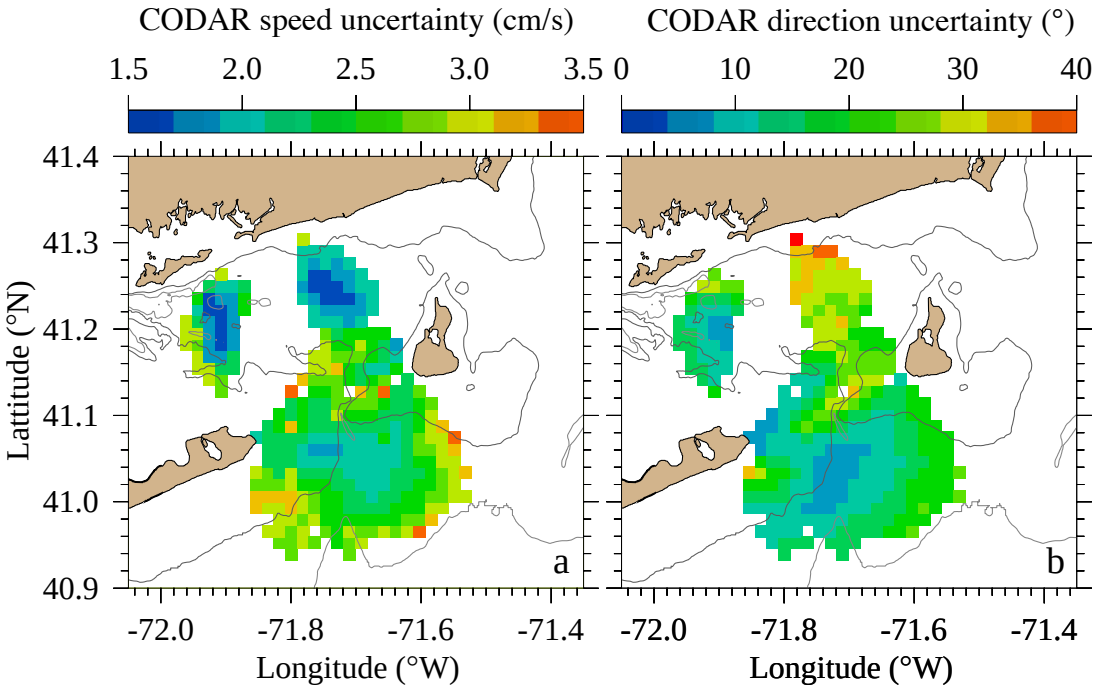

Figure 3. The distribution of the CODAR data measurement uncertainty averaged over the total hourly record at the 334 grid points. a: speed (cm/s) and b: direction (°).

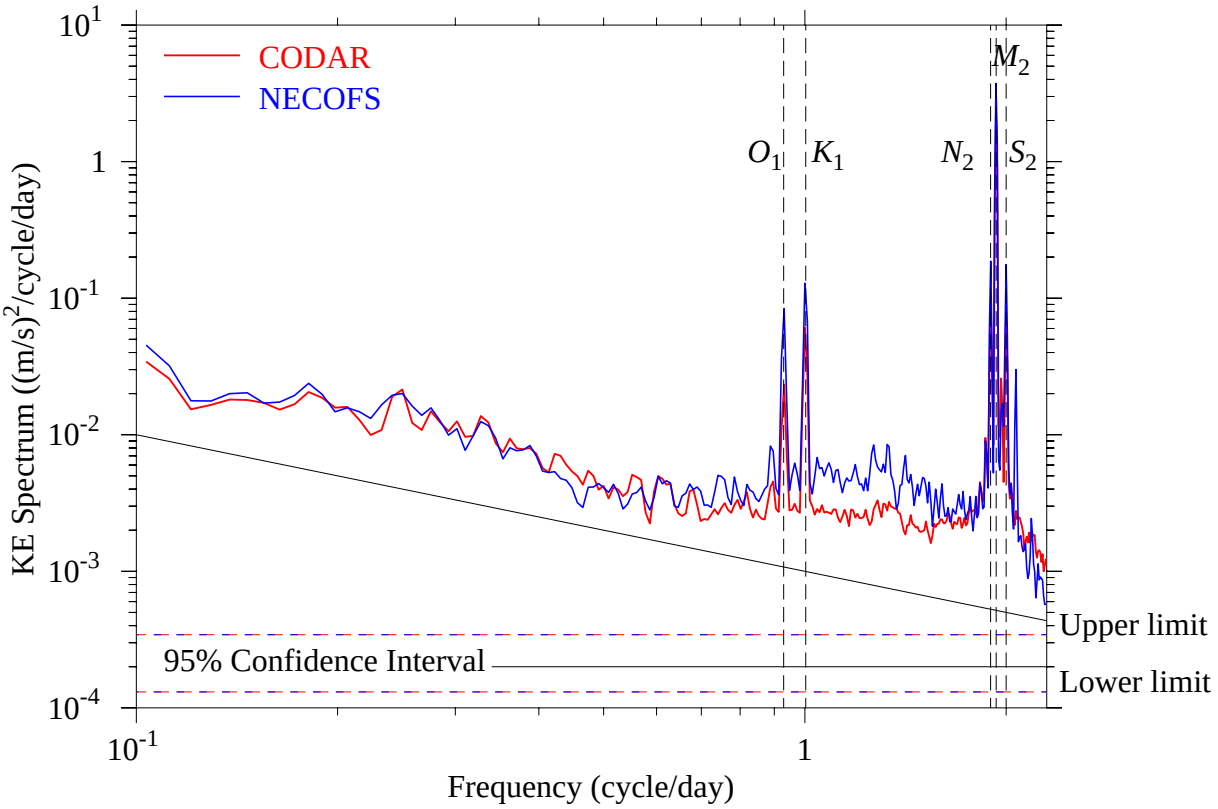

Figure 4. Comparison of CODAR-derived and NECOFS-computed current kinetic energy spectral densities averaged over 4 sites (Figure 2). The horizontal dash lines are the 95% confidence upper and lower limits (red: CODAR, blue: NECOFS). The vertical dashed lines mark the frequencies of M_2, N_2, S_2, O_1, and K_1 tidal constituents

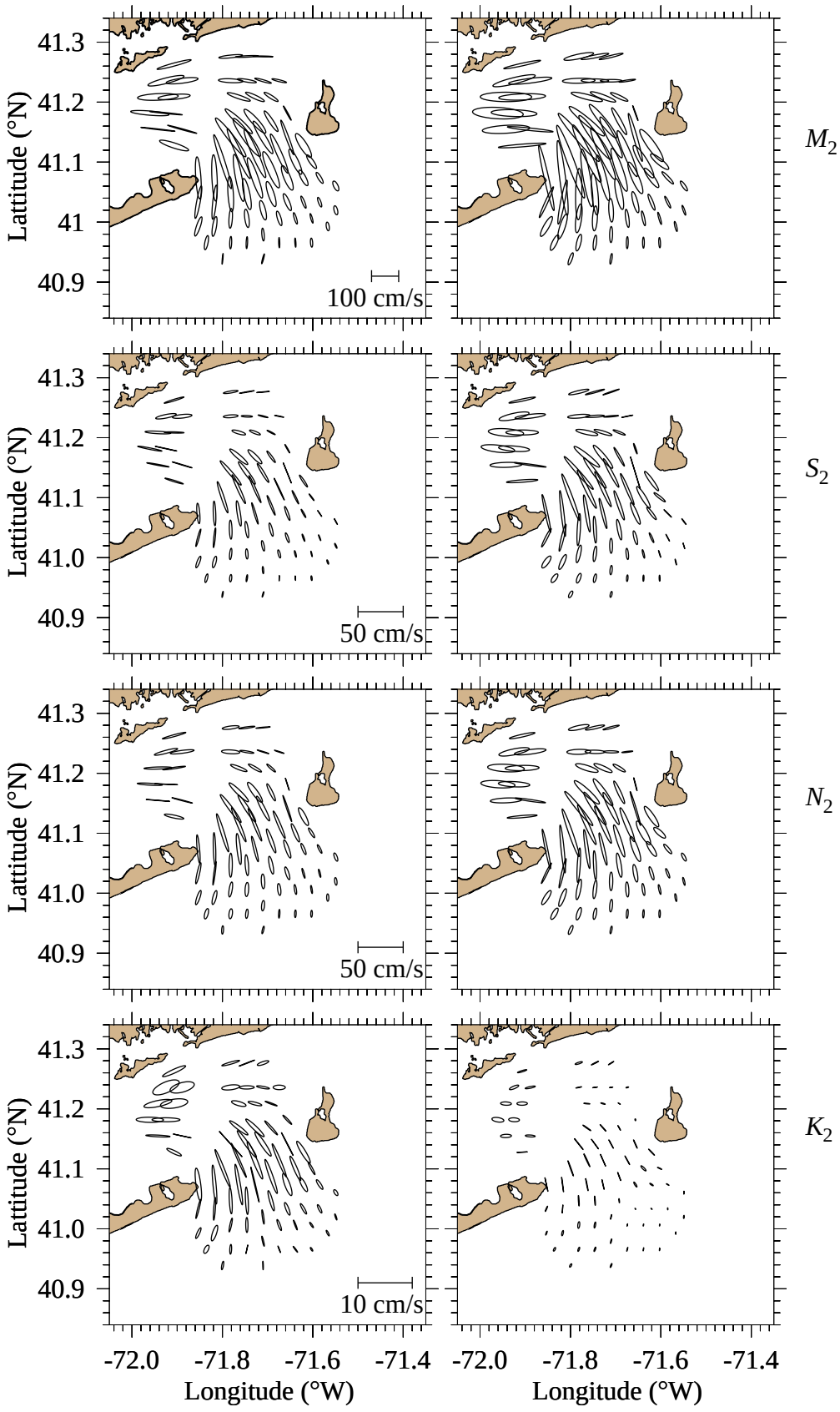

Figure 5a. Comparisons of NECOFS-computed and CODAR-derived semi-diurnal tidal current ellipses for M_2, S_2, N_2 and K_2. Left panels: CODAR-derived and right panels: FVCOM-computed.

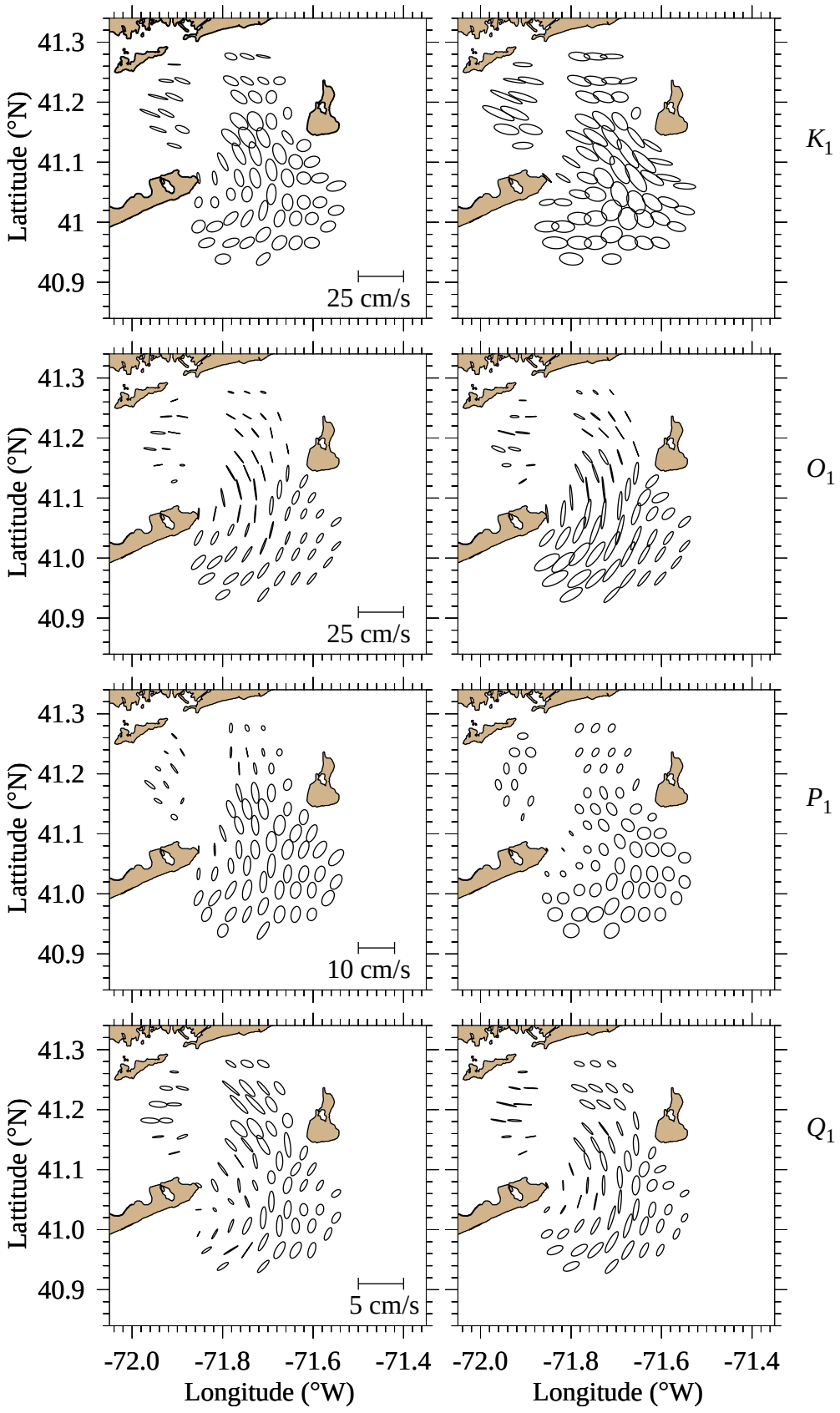

Figure 5b. CODAR-derived (left panels) and FVCOM-computed (right panels) diurnal tidal current ellipses for K_1, O_1, P_1 and Q_1.

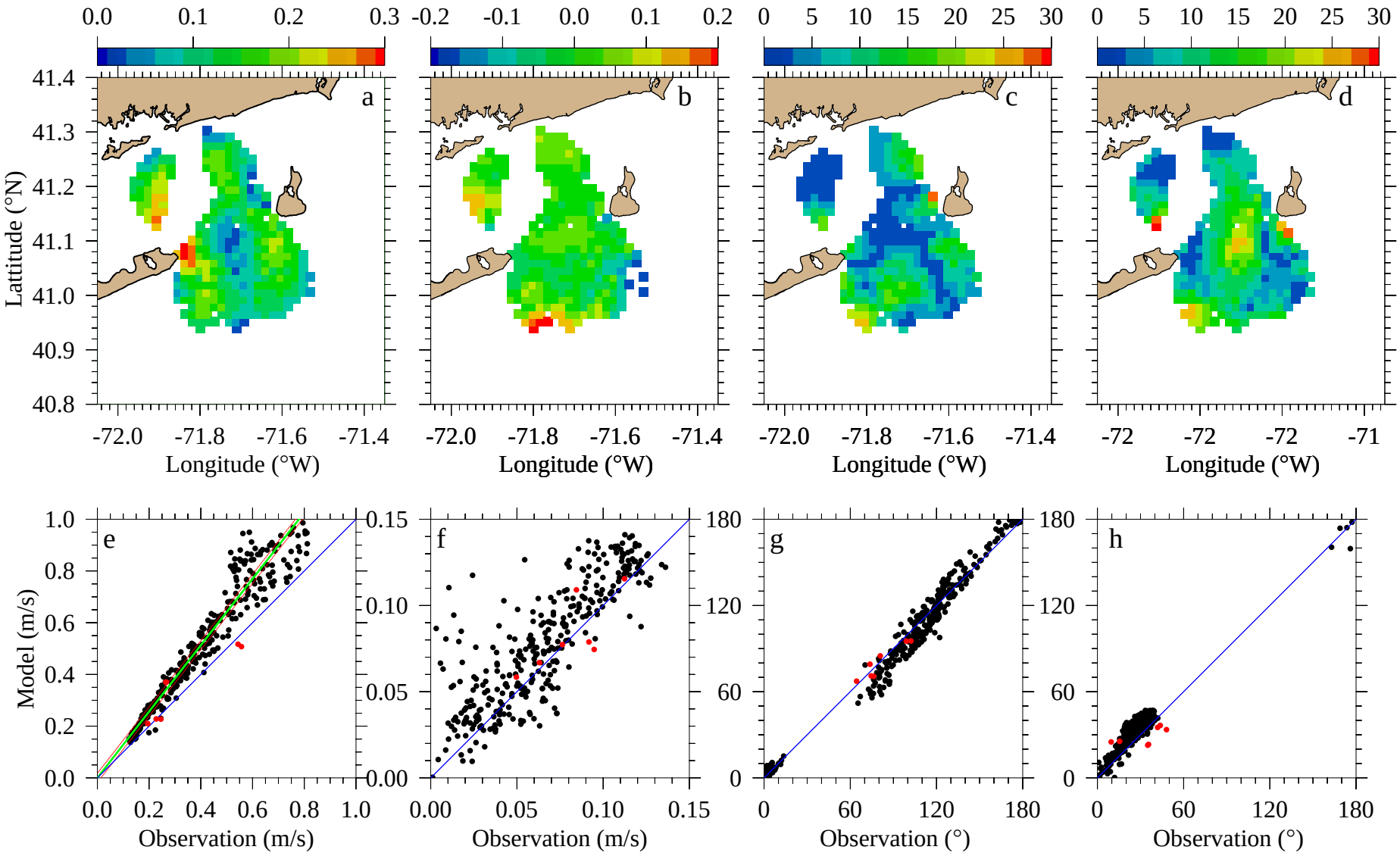

Figure 6. Upper row: distributions of differences in (a) normalized major axis, (b) eccentricity, (c) orientation (°) and (d) phase (°) calculated based on CODAR-derived and model-computed M^2 tidal currents; Lower row: scatter plots (black dots) of the CODAR-derived and model -computed (e) major axis (m/s), (f) minor axis (m/s), (g) orientation (°) and (h) phase (°) between model and CODAR (black dots). The blue line with a slope of 1 has been added in panel e for reference. The green line in panel e is the least-square fit of y=a+bx. Also shown are scatter plots (red dots) of the vertical-averaged ADCP-derived and model-computed ellipse parameters.

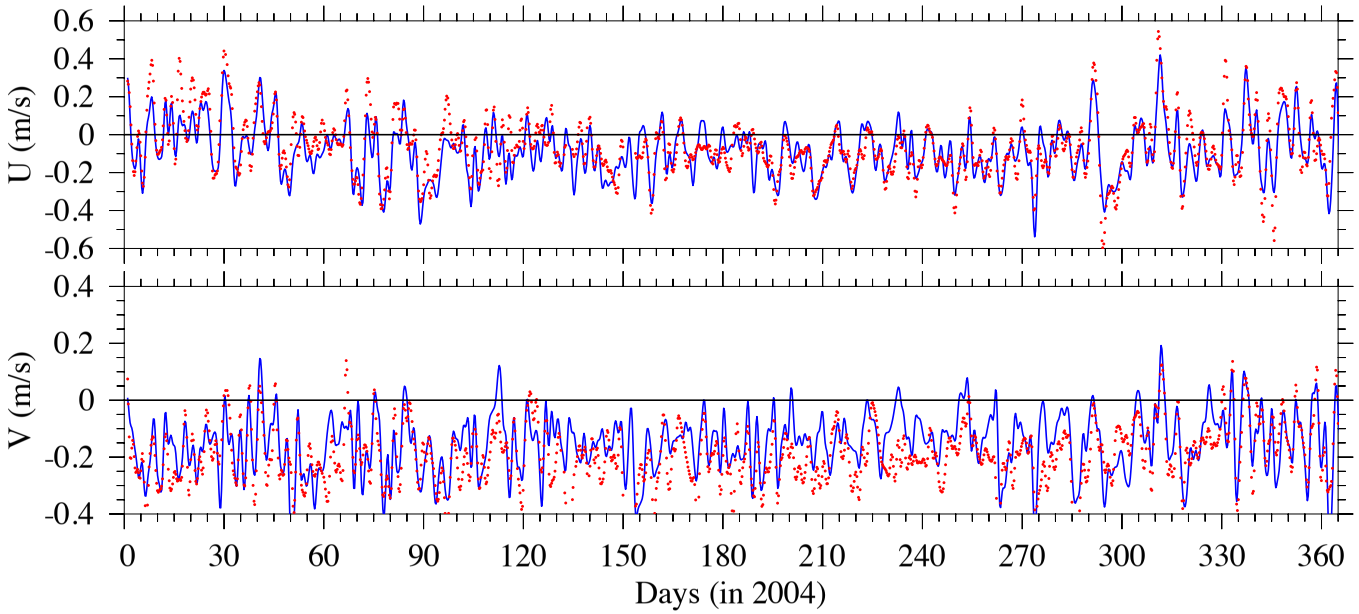

Figure 7. Subtidal current comparison between CODAR (red dots) and model (blue line) in 2004 at the circled asterisks CODAR station in Figure 2.

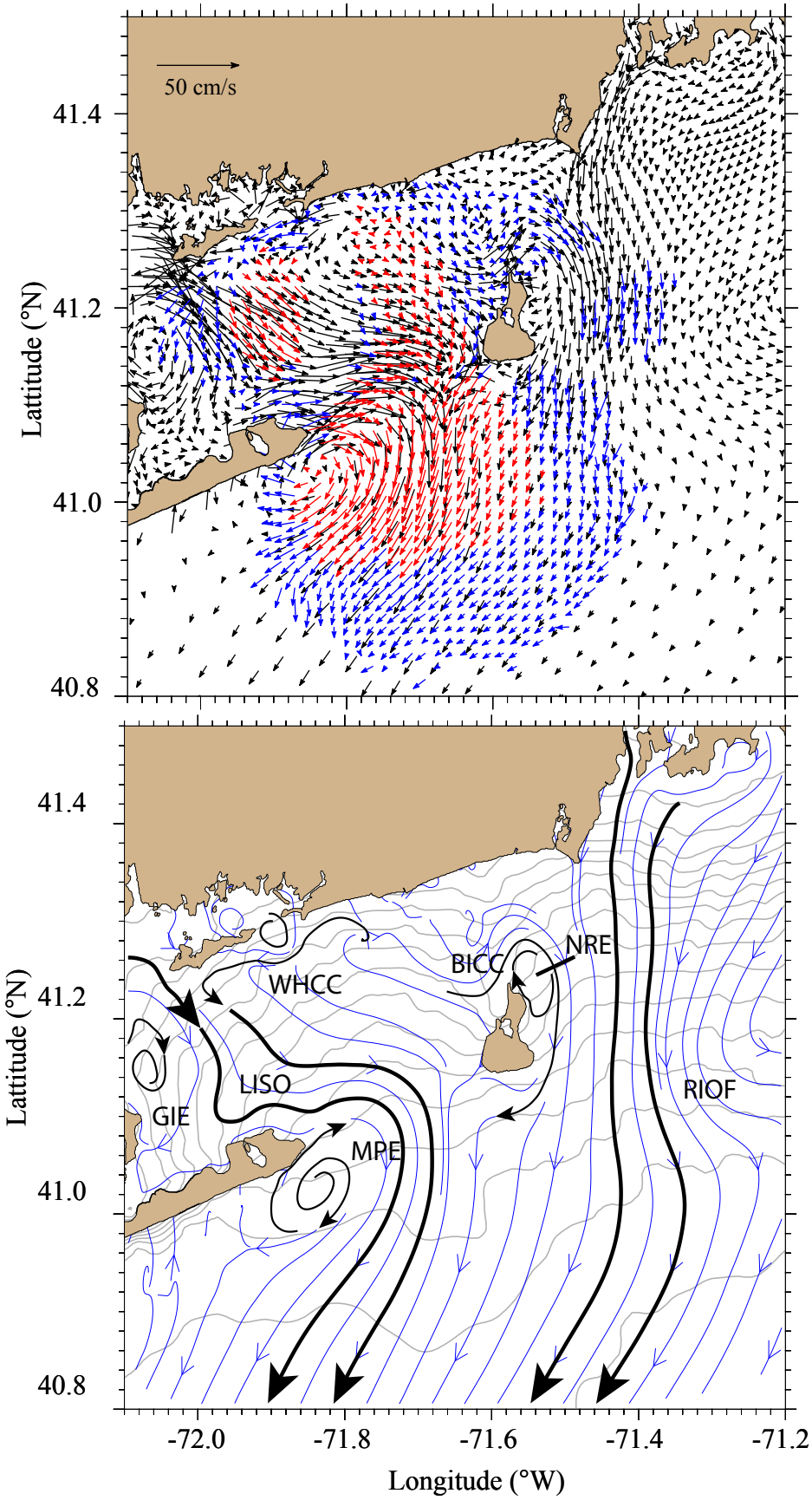

Figure 8. Upper panel: comparisons of model-computed and CODAR-derived annual mean surface currents in Block Island Sound region. Black arrows: model-computed; red arrows: CODAR-derived at the selected grid points; blue arrows: CODAR-derived at all the grid points except the 334 selected. Lower panel: The grey contours are the potential function lines. Overlaid on the streamlines is a schemtic outlining features of the flow pattern: MPE is Montauk Point Eddy; GIE is Gardiners Island Eddy; LISO is Long Island Sound Outflow; NRE is North Reef Eddy; BICC is Block Island Clockwise Circulation; WHCC is Watch Hill Coastal Current; and RIOF is Rhode Island Offshore Flow.

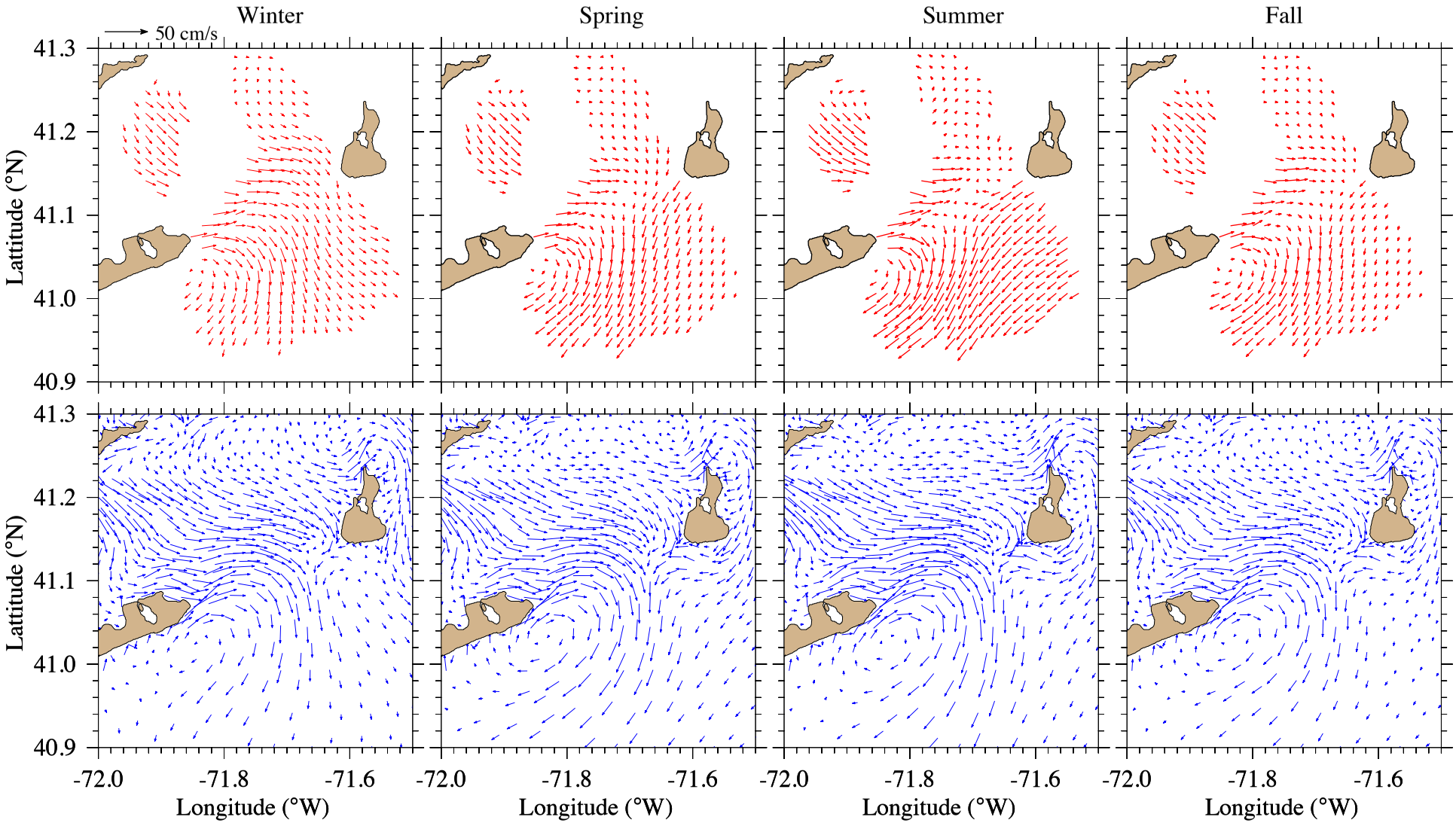

Figure 9. Comparisons of CODAR-derived (upper panels) and model-computed (lower panels) mean surface currents in winter, spring, summer and fall averaged seasonally over 2000-2008 (using only data from the 'system on' periods). Red arrows: CODAR-derived at the selected grid points; blue arrows: model-computed.

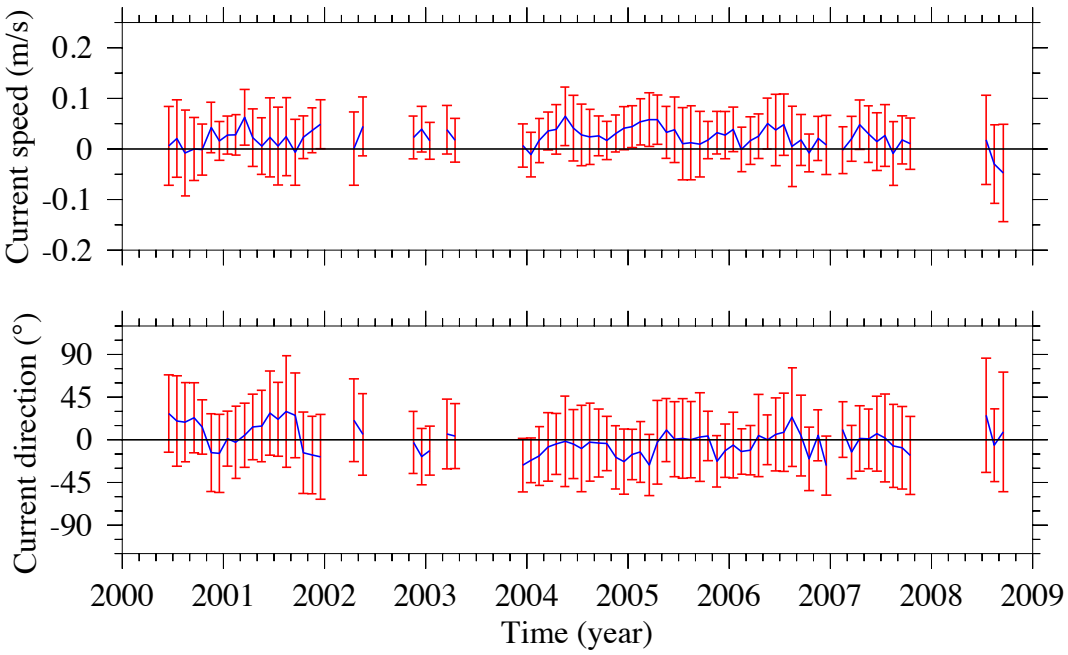

Figure 10. The difference (blue line) and standard deviation (red line) in magnitudes (upper panel) and directions (lower panel) of the 75 model-computed and CODAR-derived monthly surface velocities averaged over the 334 selected grid points from 2000 to 2008.

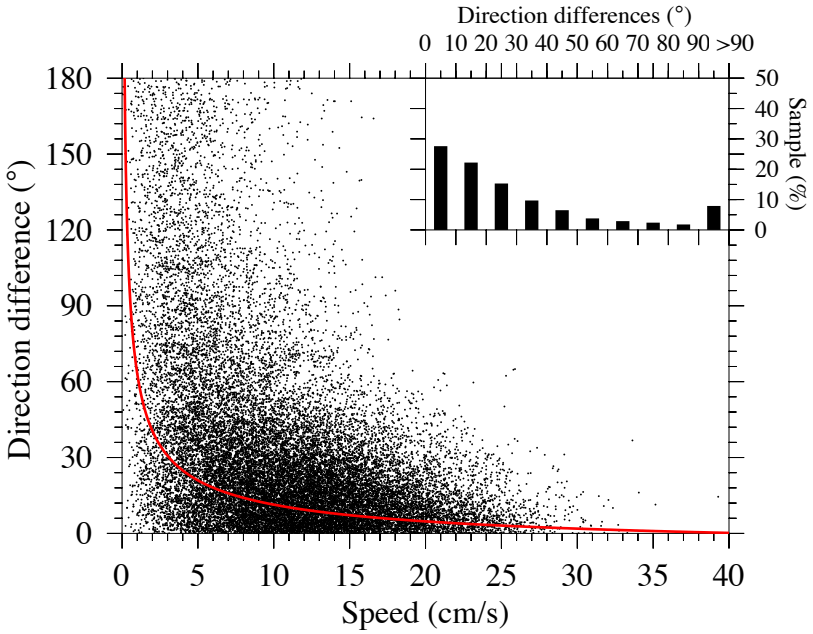

Figure 11. The larger panel shows scatter plots of the difference for the CODAR-derived and model-computed direction; the red cure is calculated from Lowess curve fitting, The upper panel shows the percentage for difference in direction.

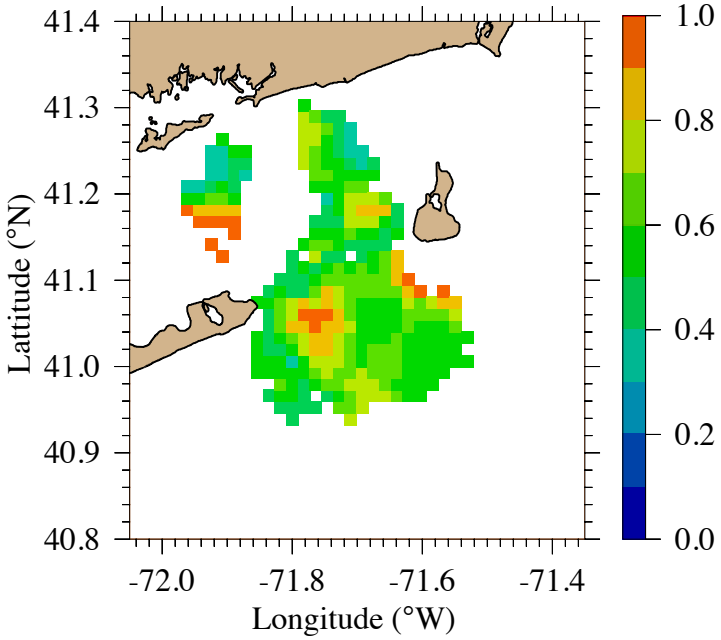

Figure 12. Distribution of the vector correlation coefficient squared ρ^2_v for the CODAR-derived and model-computed monthly surface velocity vectors. The color bar at the top is the ρ^2_v scale. Areas with $\rho^2_v > 0.22$ indicate some correlation.

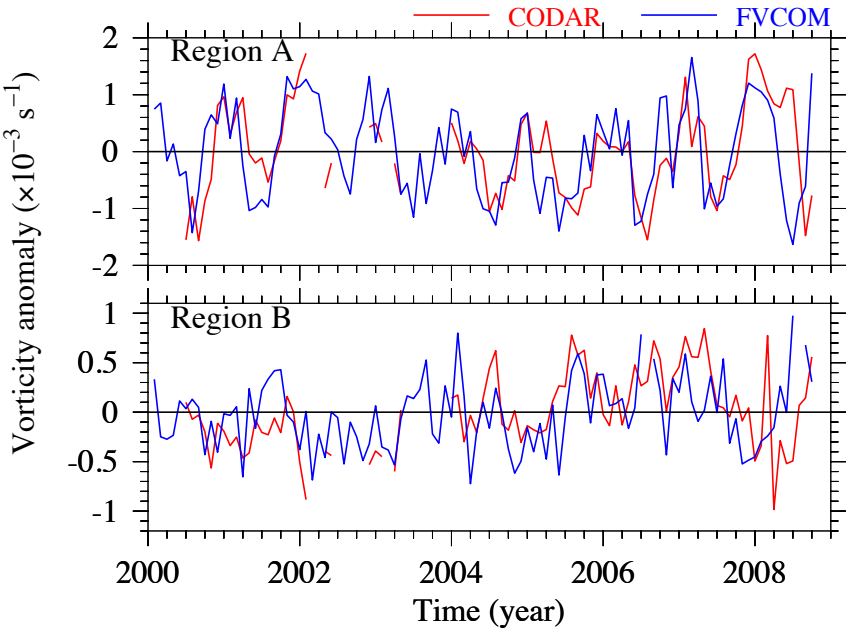

Figure 13. Comparisons of the time series of vorticity anomalies calculated from the CODAR-derived and model-computed surface velocity fields in Region A (upper panel) and Region B (lower panel).

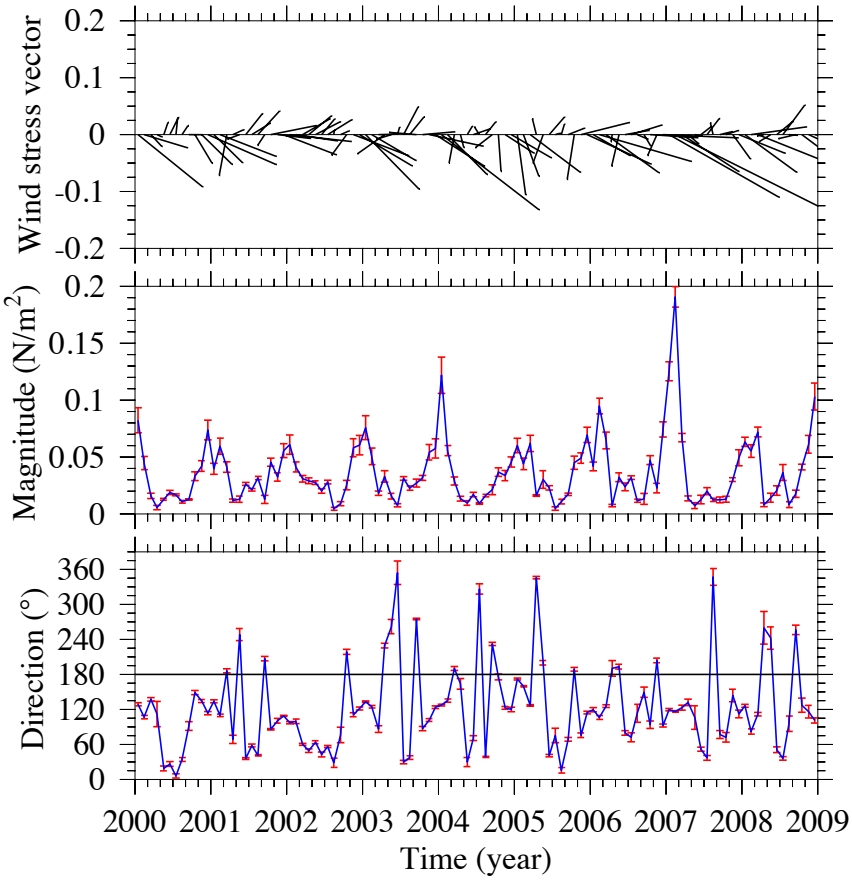

Figure 14 Time series of the monthly-mean surface wind stress vector (upper panel), its magnitude (middle panel) and direction (lower panel) averaged over sites 1-6 over the period of 2000-2008. The vertical red line segment indicates the standard deviation over the six sites for each month.

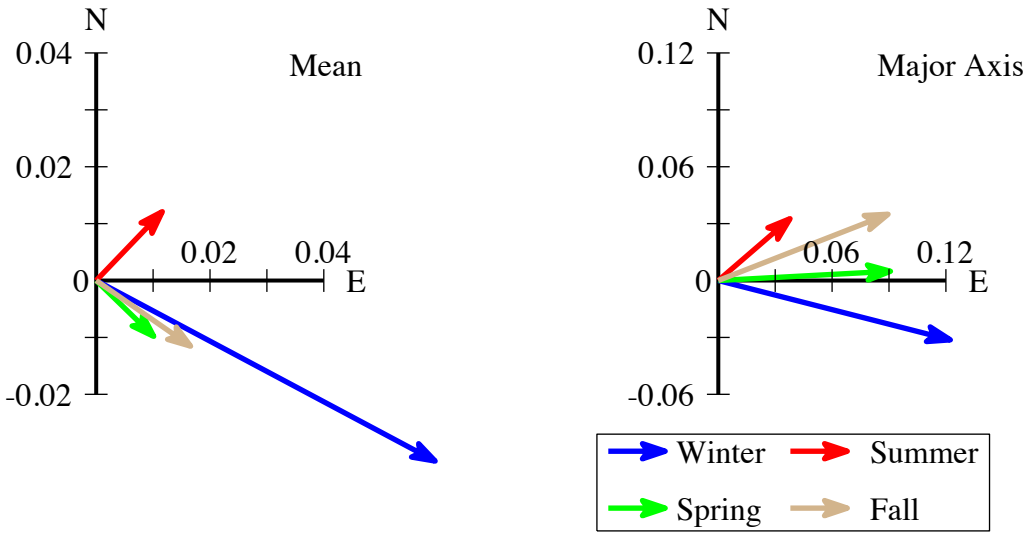

Figure 15. Mean wind stress (left panel) and major principal axis (right panel) at the six sites in the four seasons. Units: N/m^2. Note difference in scale.

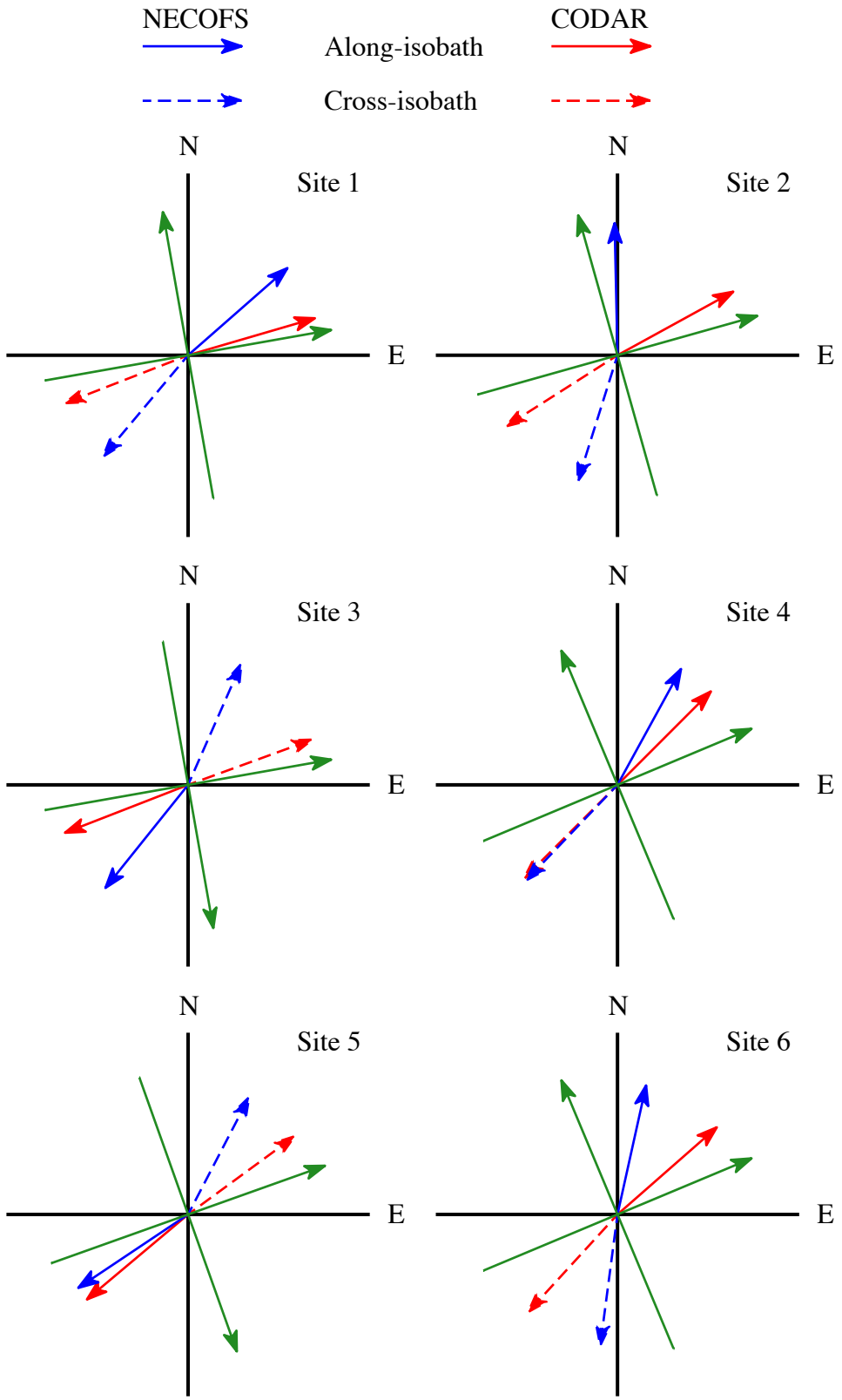

Figure 16. The direction corresponding to the maximum correlation between wind stress and the along- and cross-isobath surface current at the six sites shown in Figure 1. The along- and cross-isobath components are color coded as above. The green coordinates show the local along- and corss-isobath direction.

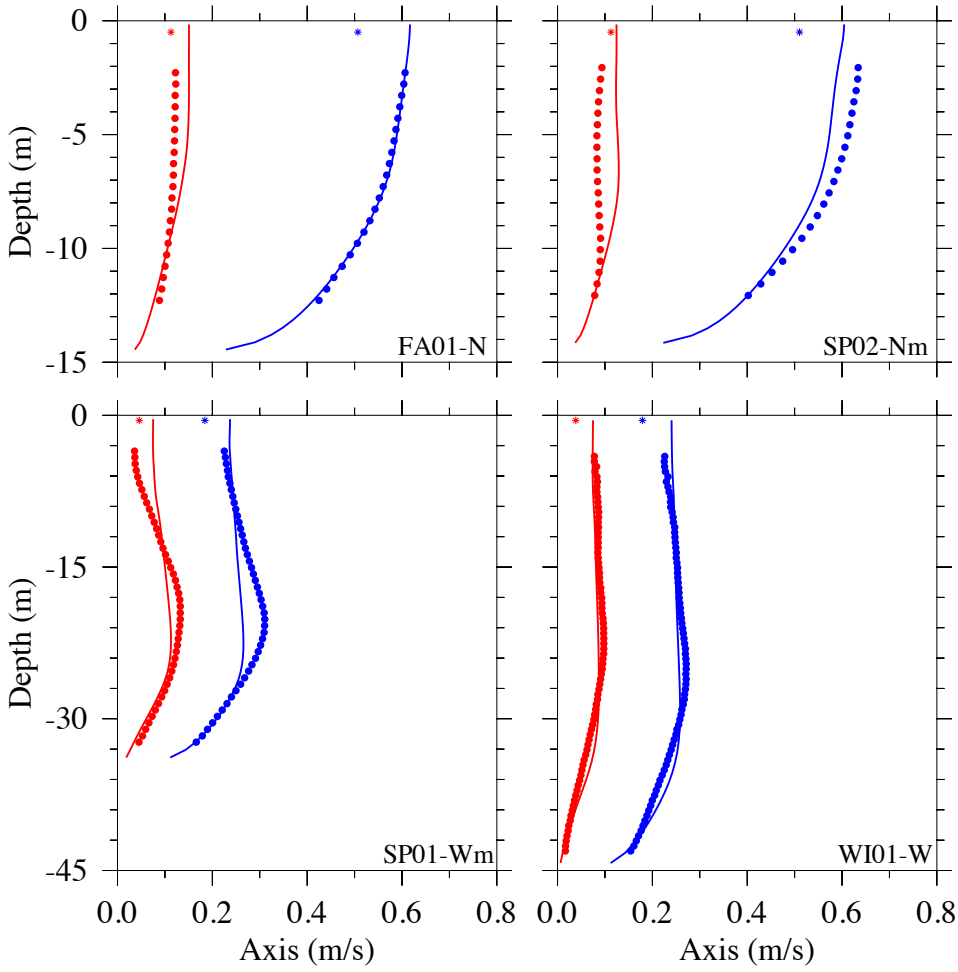

Figure 17 Vertical profile of the ADCP-derived (dots), CODAR-derived (asterisks) and model-computed (solid lines) for major axis (m/s, blue color) and minor axis (m/s, red color), based on ADCP-derived and model-computed M_2 tidal currents at 4 stations: FA01-N, SP02-Nm, SP01-Wm and WI01-W.

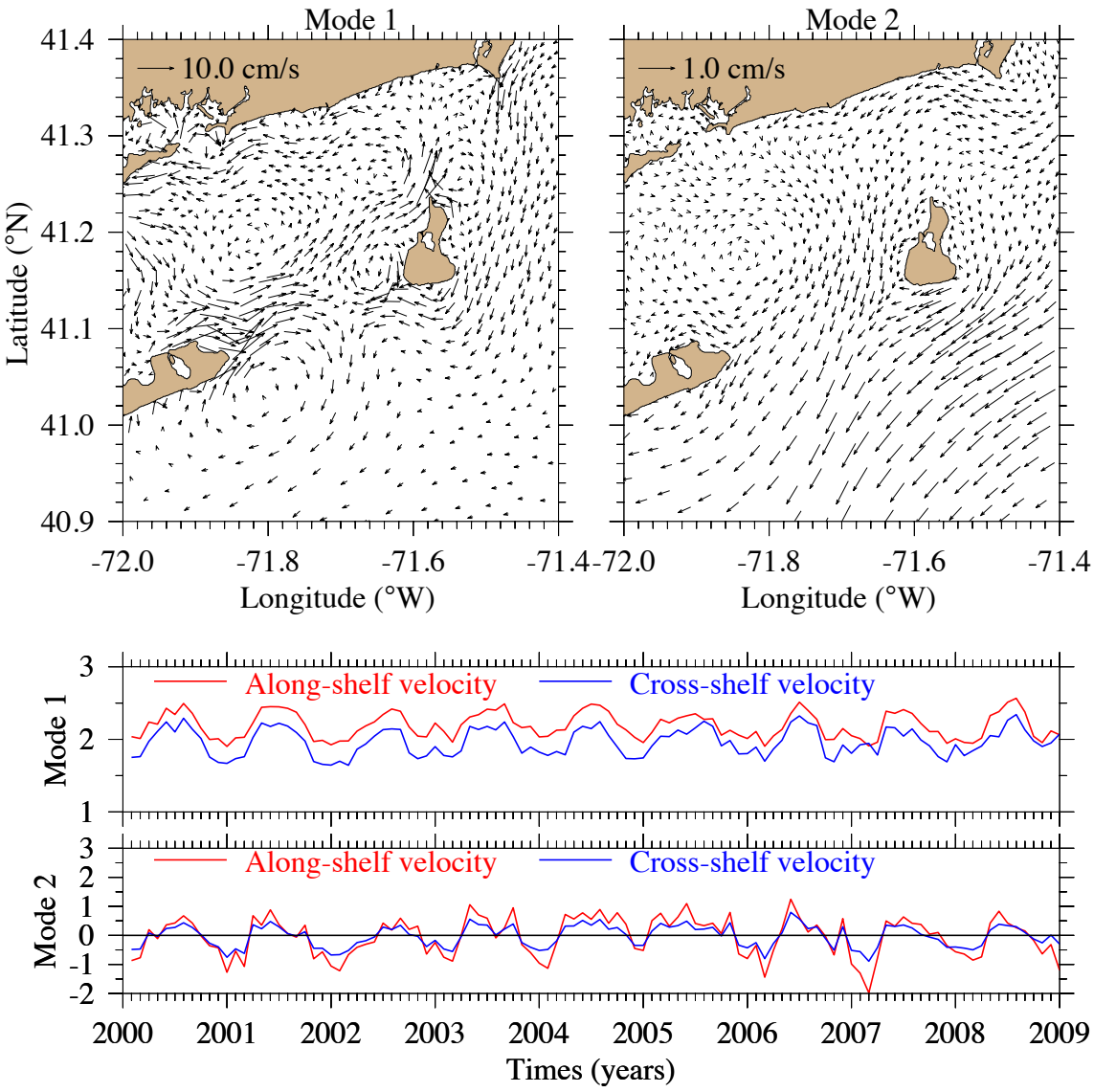

Figure 18. The two Empirical Orthogonal Function (EOF) modes dominating the flow field in Block Island Sound based on an analysis of the nine-year NECOFS vertically-averaged flow field. Upper panel: spatial distributions of the vertically-averaged velocity for the first two EOF modes. Lower panel: the the associated temporal amplitudes of the along and cross shelf velocities associated with the 1st and 2nd EOF modes.

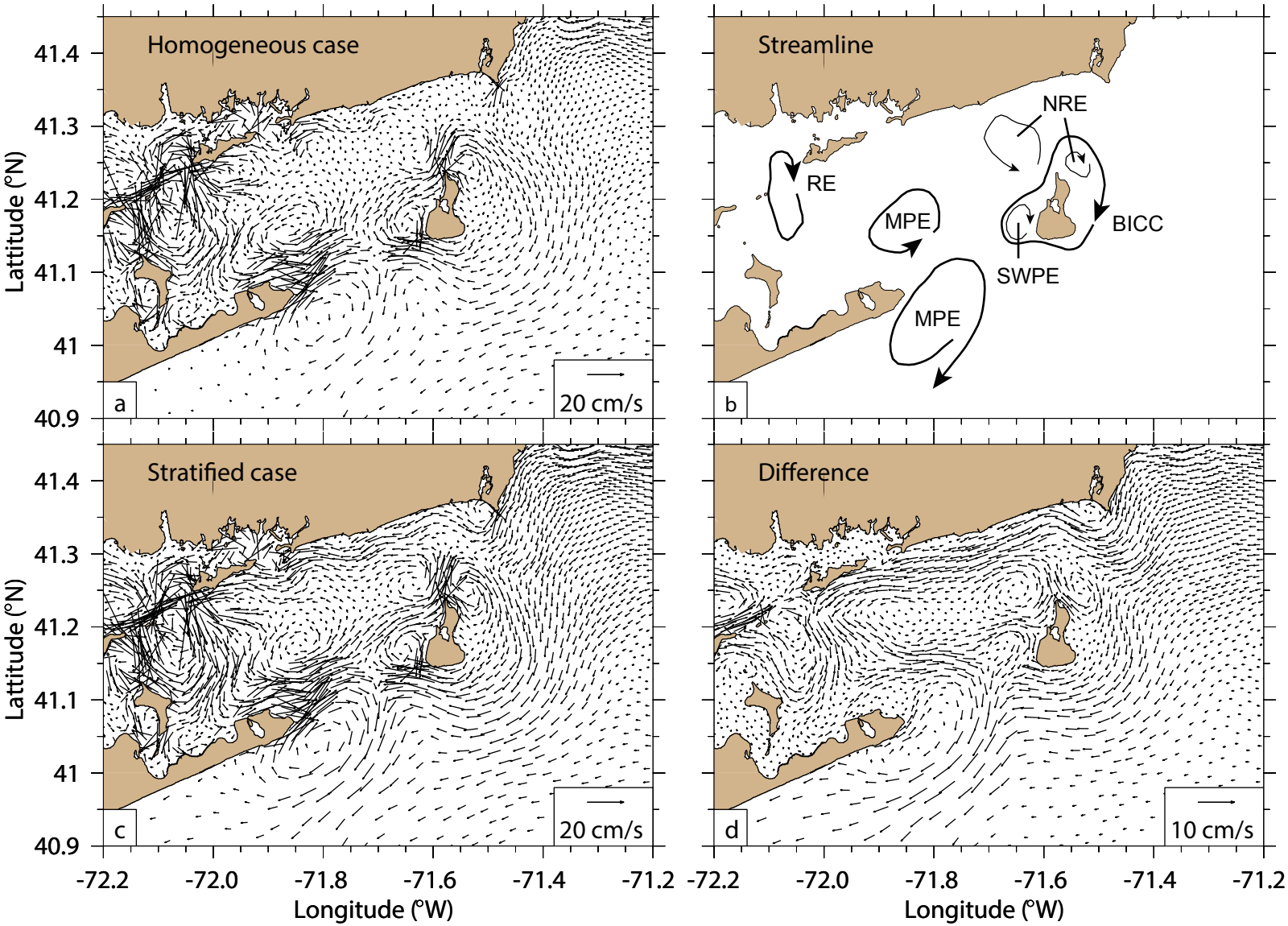

Figure 19. Distribution of the depth averaged tidal residual flow in (a) homogeneous conditions, (b) its corresponding schematic diagram, (c) tidal residual flow in summertime stratified conditions, and (d) their difference (stratified minus homogeneous cases). In (b), RE is Race Eddy; MPE is Montauk Point Eddy; NRE is North Reef Eddy; BICC is Block Island Clockwise Circulation; and SWPE is Southwest Point Eddy.

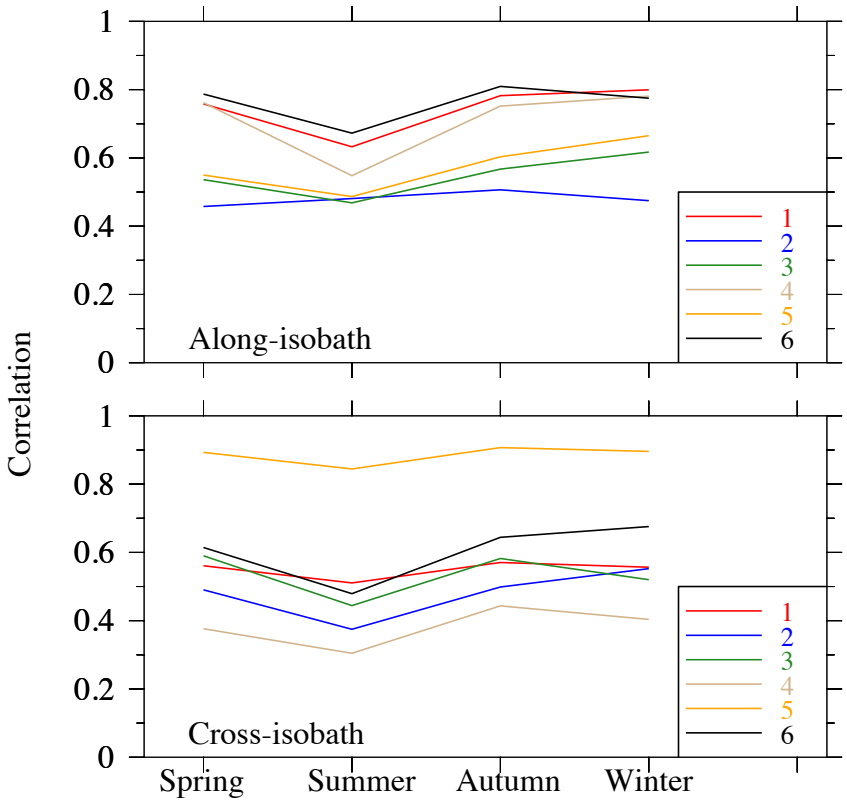

Figure 20. Seasonal variability of the maximum wind-current correlation coefficient at sites 1-6, the along-isobath velocity in upper panel and the cross-isobath velocity in lower panel. The correlation coefficient is a seasonally-averaged value over the period 2000-2008.

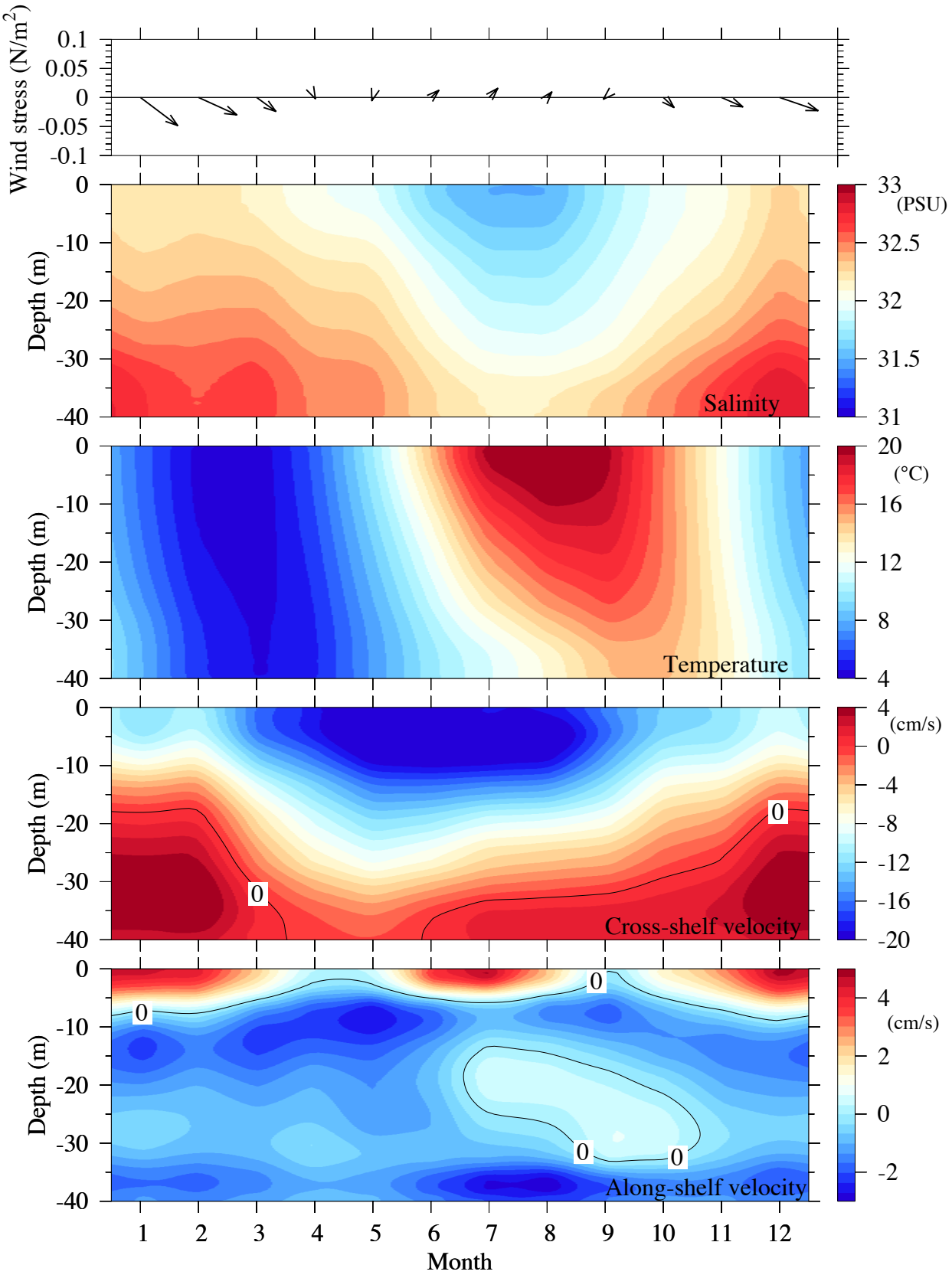

Figure 21. Nine-year averaged wind stress, salinity, temperature profile at site 6, cross-shelf velocity profile (positive is onshore toward the north), along-shelf velocity profile (positive is along-shelf toward the west).

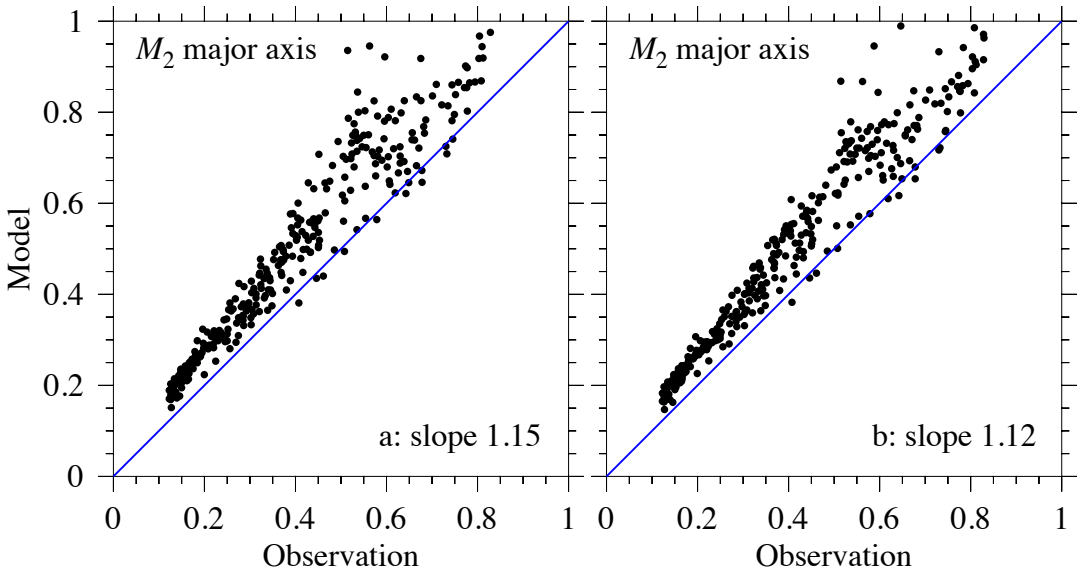

Figure 22. Scatter plots of the CODAR-derived and model-computed major axes of the M_2 tidal current (m/s). (a): for the case with the updated bathymetry; (b): for the case with an increased bottom roughness. The blue line with a slope of 1 has been added for reference. The slope of the least-squares linear fit to the data is shown in the lower right of each panel.